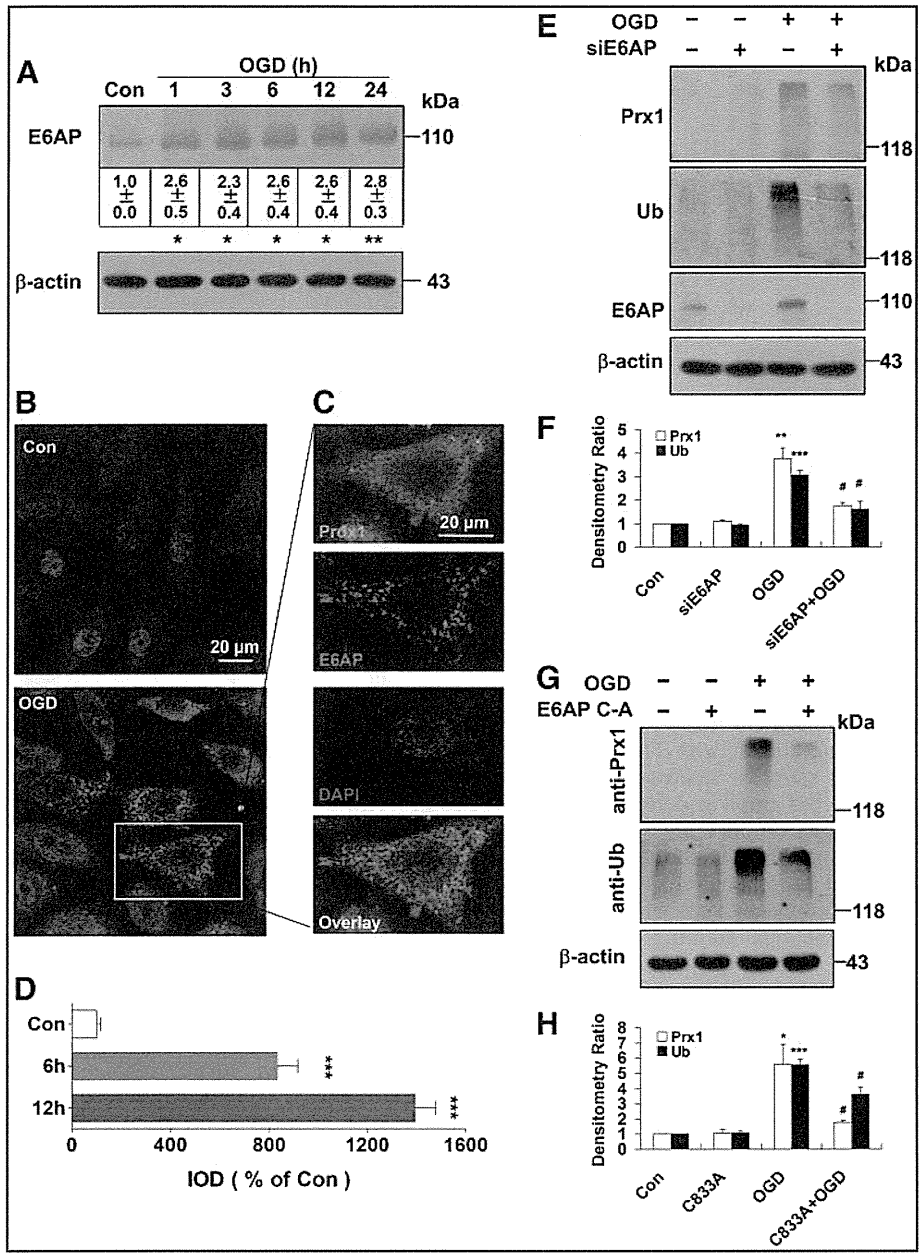


**FIG. 5. E6AP activation contributes to the Prx1 stress response after OGD.** **(A)** The representative image showing E6AP activation at the indicated time points after OGD treatment. Data are expressed as densitometry ratio of control (mean ± SEM). $*p<0.05$; $**p<0.01$ *versus* control. **(B)** Immunocytochemical analysis of E6AP expression after OGD treatment. Laser confocal microscopy demonstrated low to undetectable levels of E6AP in control cells. **(C)** Higher-magnification image of endothelial staining from the *insets* of **(B)**. DAPI counterstaining indicates nuclear localization (blue). Scale bar = 20 μm. **(D)** Quantification of Prx1 immunofluorescence expressed as integrated optical density (IOD). $***p<0.001$ *versus* control. **(E)** *E6AP* knockdown reduced the OGD-induced formation of multiubiquitinylated proteins. Cells were submitted to *E6AP* knockdown and OGD or the control condition for 6 h. Cell lysates were prepared and resolved by SDS-PAGE. The proteins were immunoblotted with antibodies against Prx1, E6AP, and ubiquitin. **(F)** Quantitative analyses for **(E)** are shown in the bar graph as densitometry ratio of control (mean ± SEM). $**p<0.01$; $***p<0.001$ *versus* control; $^{\#}p<0.05$ *versus* OGD. **(G)** The $E6AP_{C\text{-}A}$ mutant decreased OGD-induced Prx1 ubiquitination in endothelial cells. EA.hy926 cells were cultured and transfected with plasmid DNA encoding the $E6AP_{C\text{-}A}$ mutant or an empty plasmid using Attractene. **(H)** Quantitative analysis of protein levels for **(G)** was performed by densitometry. Data are expressed as densitometry ratio of control (mean ± SEM). $*p<0.05$; $***p<0.001$ *versus* control; $^{\#}p<0.05$ *versus* OGD. Immunodetection of β-actin was used as a loading control. Immunoblots are representative of three independent experiments. E6AP, E6-associated protein. To see this illustration in color, the reader is referred to the web version of this article at www.liebertpub.com/ars

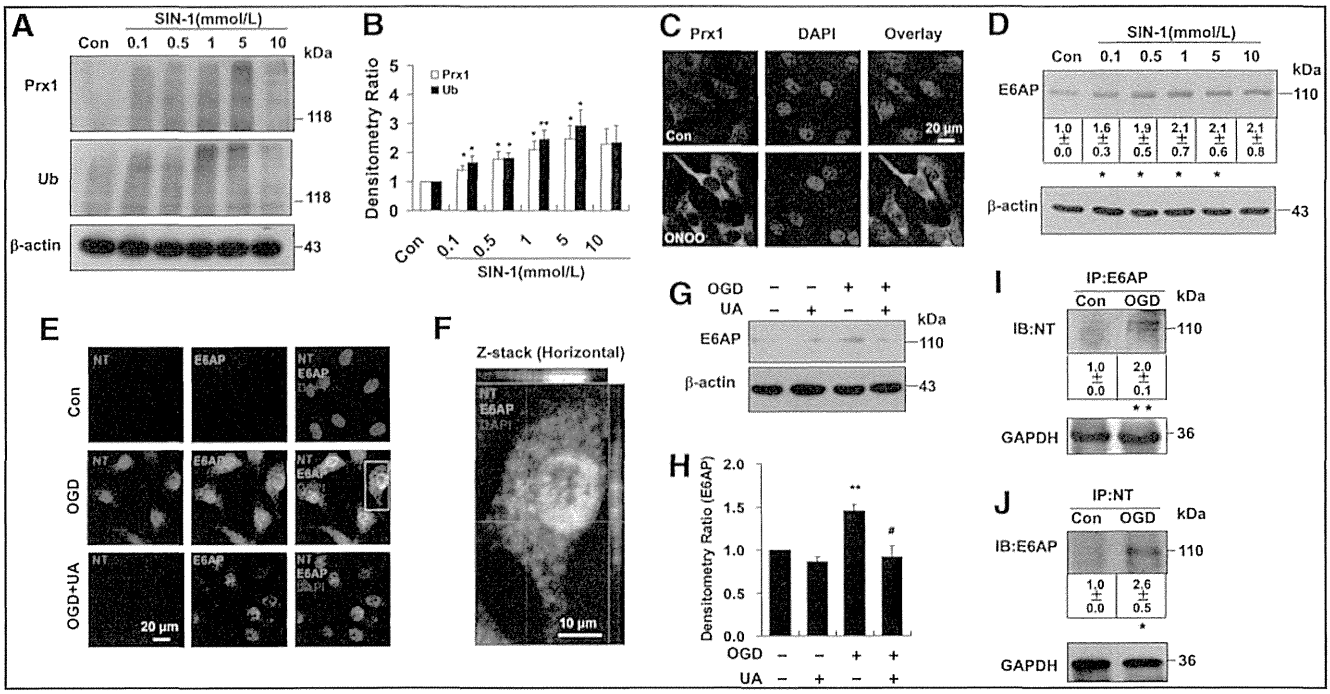


**FIG. 6. Nitrosative stress is associated with ubiquitination of Prx1 in endothelial cells.** **(A)** The ubiquitination of Prx1 after SIN-1 stimulation in endothelial cells. The blots were labeled with anti-Prx1 or anti-ubiquitin antibody and visualized with the ECL system. Molecular sizes are indicated on the *right*. **(B)** The SIN-1-induced changes in polyubiquitinated Prx1 were quantified and shown in the bar graph as densitometry ratio of control (mean ± SEM). $*p < 0.05$; $**p < 0.01$ *versus* control. **(C)** Immunocytochemical analysis of Prx1 level after $ONOO^-$ treatment by laser confocal microscopy. DAPI counterstaining indicates nuclear localization (blue). **(D)** The effects of SIN-1 treatment on E6AP protein levels were examined in cell lysates of endothelial cells. EA.hy926 endothelial cells were cultured with or without SIN-1 treatment for 6 h at the indicated concentrations. Immunoblots are representative of three independent experiments (mean ± SEM). $*p < 0.05$ *versus* control. **(E)** Fluorescence immunocytochemical staining of E6AP and nitrotyrosine 6 h after OGD in endothelial cells with or without 0.5 m*M* uric acid treatment. DAPI counterstaining indicates nuclear localization (blue). NT, nitrotyrosine; UA, uric acid. **(F)** Higher-magnification image of endothelial staining from the *insets* is shown in **(E)**. **(G)** Effect of uric acid on E6AP expression in endothelial cells following OGD. Immunodetection of $\beta$-actin was used as a loading control. **(H)** Quantification of E6AP protein levels was performed using densitometric analysis of the immunoblots in **(G)**. Immunoblots are representative of three independent experiments. Data are expressed as the percentage of values of control (mean ± SEM). $**p < 0.01$ *versus* control; $^{\#}p < 0.05$ *versus* OGD. **(I)** Immunoprecipitation of E6AP from cell lysates of OGD-treated endothelial cells followed by blotting with an anti-nitrotyrosine antibody. $**p < 0.01$ *versus* control. **(J)** The OGD-induced nitration of E6AP was detected by the immunoprecipitation of nitrotyrosine followed by immunoblotting with an anti-E6AP antibody. Immunoblots are representative of three independent experiments (mean ± SEM). $*p < 0.05$ *versus* control. SIN-1, 3-morpholinosydnonimine. To see this illustration in color, the reader is referred to the web version of this article at www.liebertpub.com/ars

striatum (Supplementary Figs. S9 and S10). Staining of brain sections from lentiviral-*GFP*-injected mice with a neuronal nuclear marker (NeuN) (Fig. 8B-d) and an endothelial marker CD31 (Fig. 8B-e, f) indicates that the vector successfully transduced cells in the brain. Although the lentiviral vectors might directly diffused into the brain parenchyma, the present data indicate that lentiviral vectors in cerebral ventricular can diffuse along the neurovascular scaffold. Immunohistochemical analysis of ipsilateral sections revealed stronger GFP fluorescence in tMCAO mice that formed a continuous interendothelial staining pattern that colocalized with CD31 (Fig. 8C, D).

The protective effects of Prx1 against ischemia-induced neurological and functional deficit were evaluated by the rotarod test and neurological score measurements. The neurological scores were decreased significantly, and rotarod time was increased in LV-*Prx1*-treated mice 24 h after tMCAO (Fig. 9A) and the infarct area was reduced accordingly (Fig. 9B). The breakdown products of spectrin and calcineurin were increased after tMCAO (Fig. 9C, D), coincident with BBB leakage (Fig. 9E, F). LV-*Prx1* treatment blocked the degradation of tight junction proteins zonula occludens-1 (ZO-1) and claudin5 (Fig. 9C, D, and G) and significantly reduced BBB leakage (Fig. 9E, F). LV-*Prx1* transduction reduced the $O_2^{\bullet -}$ level assessed from dihydroethidium staining in the penumbra region of mice 24 h after tMCAO (Fig. 9H, I).

### *Schematic illustration of the mechanisms by which nitrosative stress induces Prx1 ubiquitination during ischemic insult in endothelial cells*

We hypothesize that ischemia-induced nitrosative stress causes an early increase in Prx1 production during the adaptive phase, whereas excessive or prolonged ischemia activates E6AP E3 ubiquitin ligase, which targets Prx1 for ubiquitination and degradation during the late phase, thereby degrading the Prx1-related antioxidant defense pathway and

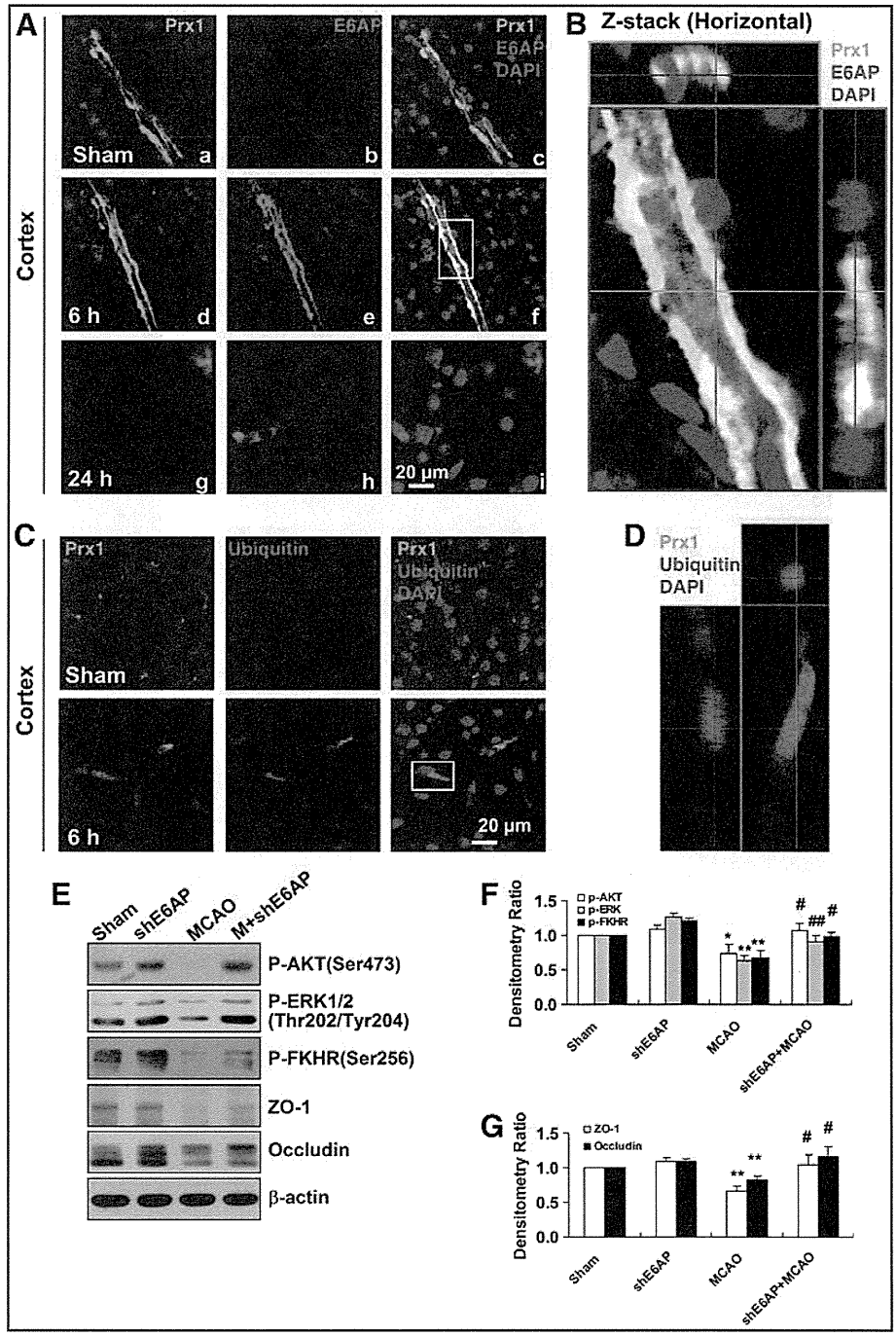


**FIG. 7. E6AP activation is associated with Prx1 ubiquitination in brain microvessels of cerebral ischemia mice.** **(A)** Double immunohistochemical staining for Prx1 and E6AP in the penumbra after tMCAO. Fluorescence staining for Prx1 (green) and E6AP (red) was performed in ipsilateral brain regions 6 and 24 h after brain ischemic injury in mice. **(B)** The orthogonal projections onto the $x-z$ (*upper*) and $y-z$ (*right*) planes are shown to confirm the colocalization of Prx1 and E6AP throughout the microvessels shown in **(A)**. **(C)** Fluorescence immunohistochemical staining of Prx1 and ubiquitin in brain microvessels. Anti-ubiquitin (red) and Prx1 (green) staining was performed 6 h after tMCAO in mice. **(D)** Higher-magnification image of endothelial staining from the *insets* is shown in **(C)**. Each image shown is representative of five independent mice. **(E)** The effect of *E6AP* knockdown on neurovascular damage after brain ischemia in mice. The lentivirus *E6AP* shRNA knockdown was used to silence *E6AP* mRNA. The protein extracts from penumbra brain region of mice were processed for Western blotting to detect ZO-1, Occludin, and phosphorylated AKT, ERK, FHHR. **(F, G)** Quantitative analysis of protein levels in **(E)** was performed by densitometry. Densitometry values were normalized to the average of all sham values (mean ± SEM, $n=6$). $^{*}p<0.05$; $^{**}p<0.01$ *versus* sham mice; $^{\#}p<0.05$; $^{\#\#}p<0.01$ *versus* vehicle-treated mice. Immunoblotting with an anti-β-actin antibody demonstrated equal protein loading in each lane. tMCAO, transient middle cerebral artery occlusion; ZO-1, zonula occludens-1; shRNA, short hairpin RNA. To see this illustration in color, the reader is referred to the web version of this article at www.liebertpub.com/ars

rendering the endothelial cells in the microvessels susceptible to ischemic damage (Fig. 10).

## Discussion

The present study demonstrates that in endothelial cells OGD treatment leads to oxidative and nitrosative stress that engage an early increase in Prx1 production and an antioxidant response. However, more prolonged or severe ischemia-mediated nitrosative stress ubiquitinates Prx1 by the activation of E6AP ligase, thereby degrading this antioxidant defense pathway. The translational studies in mice after MCAO demonstrated that neurovascular protection was coordinated by active Prx1.

Prx1 initiates the antioxidant response by scavenging free radicals formed in response to a diverse array of cellular stresses (40, 44). Upregulation of Prx1 may be secondary to the activation of NF-E2-related factor 2 (Nrf2) (24), as *Prx1* promoter has two antioxidant response elements that are putative binding sites for Nrf2. Indeed, we recently demonstrated that Nrf2 signaling coordinates the defense against ischemia/nitrosative stress in endothelial cells (49).

The ubiquitin–proteasome system is important for protein degradation in eukaryotic cells (19, 42). Unexpectedly, ubiquitin was not highly expressed in control endothelial cells, but high-molecular-weight Prx1-polyubiquitin ladders were observed after OGD or SIN-1 treatment. The aggregation of

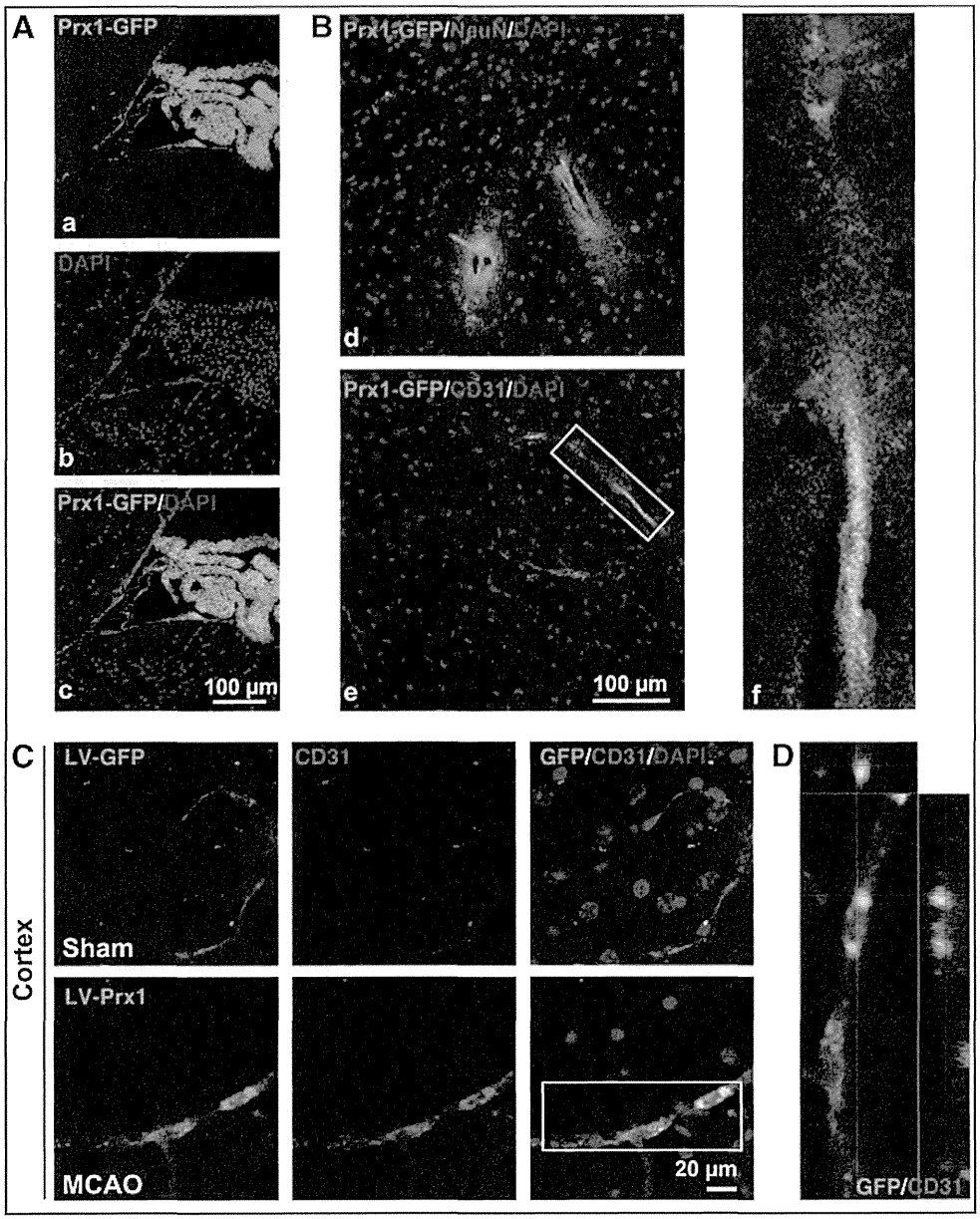


**FIG. 8. The brain microvessels are the primary cell type transduced by the LV-*GFP* vector in the ipsilateral side of tMCAO mice.** (**A**) The distribution of LV-GFP-Prx1 in the choroid plexus of the mouse brain 2 weeks after intracerebroventricular injection. Images demonstrate successful LV-*GFP-Prx1* transduction in choroid plexus cells. (**B**) The immunohistochemical localization of NeuN-labeled cells (red) in (**d**) and CD31-marked cells (red) in (**e**) were examined in brain cortex of mice. The *inset* (**f**) showing magnified images from (**B-e**) demonstrates the localization of GFP-Prx1 in the microvessels of the brain. (**C**) Representative immunostaining demonstrates that CD31 (red) colocalized with GFP-Prx1 on the ipsilateral side of the brain cortex 24 h after MCAO. (**D**) Representative Z-stack images shown in (**C**). Each image shown is representative of five independently injected mice. NeuN, neuronal nuclear marker. To see this illustration in color, the reader is referred to the web version of this article at www.liebertpub.com/ars

ubiquitinylated Prx1 proteins in endothelial cells after OGD reflects an imbalance between the amount of toxic unfolded proteins and the capacity of the proteasomal system to eliminate them, which may culminate in ER stress. Consistent with our *in vitro* data, there was an increased ubiquitination of Prx1 in brain microvessels of mice following MCAO that was associated with endothelial/microvessel injury. The formation of ubiquitin–protein conjugates (ubi-proteins) may mediate ischemic cell death (19, 51). A time-dependent increase in E6AP after OGD induced Prx1 ubiquitination (33). The upregulation and colocalization of E6AP with Prx1 after OGD was blunted by inhibition of nitrosative stress with uric acid or FeTPPS.

Our results identify E6AP as the E3 ligase that targets Prx1 for degradation in the later phases of OGD. Accordingly, we tested the functional relevance of this pathway in protecting the BBB of mice during tMCAO. Brain ischemia increased E6AP expression in microvessels of the penumbra region. Nitrosative stress from the reaction of NO generated by NO synthases in damaged brain cells and $O_2^{\bullet -}$ generated during ischemia underlays the ischemic cerebral cell death (17, 48). We speculate from our endothelial cell model that ischemic nitrosative stress induced the overproduction of brain microvascular E6AP. Indeed, the computational predictor evaluated 7 potential tyrosine nitration sites of E6AP with high score (Supplementary Fig. S11). Additionally, *S*-nitrosylation has been shown to modify the function of many proteins (1, 32). Therefore, it will also be important to further characterize the protein *S*-nitrosylation of thiol and amine groups during ischemia in the future.

Our finding that inhibition of nitrosative stress and redirection of E6AP restored Prx1 signaling in endothelial cells defines a new vasoprotective mechanism against the damaging consequences of ischemia. This was exemplified by the demonstration that Prx1 overexpression in the intact brain blocked tMCAO-induced neurovascular damage, attenuated

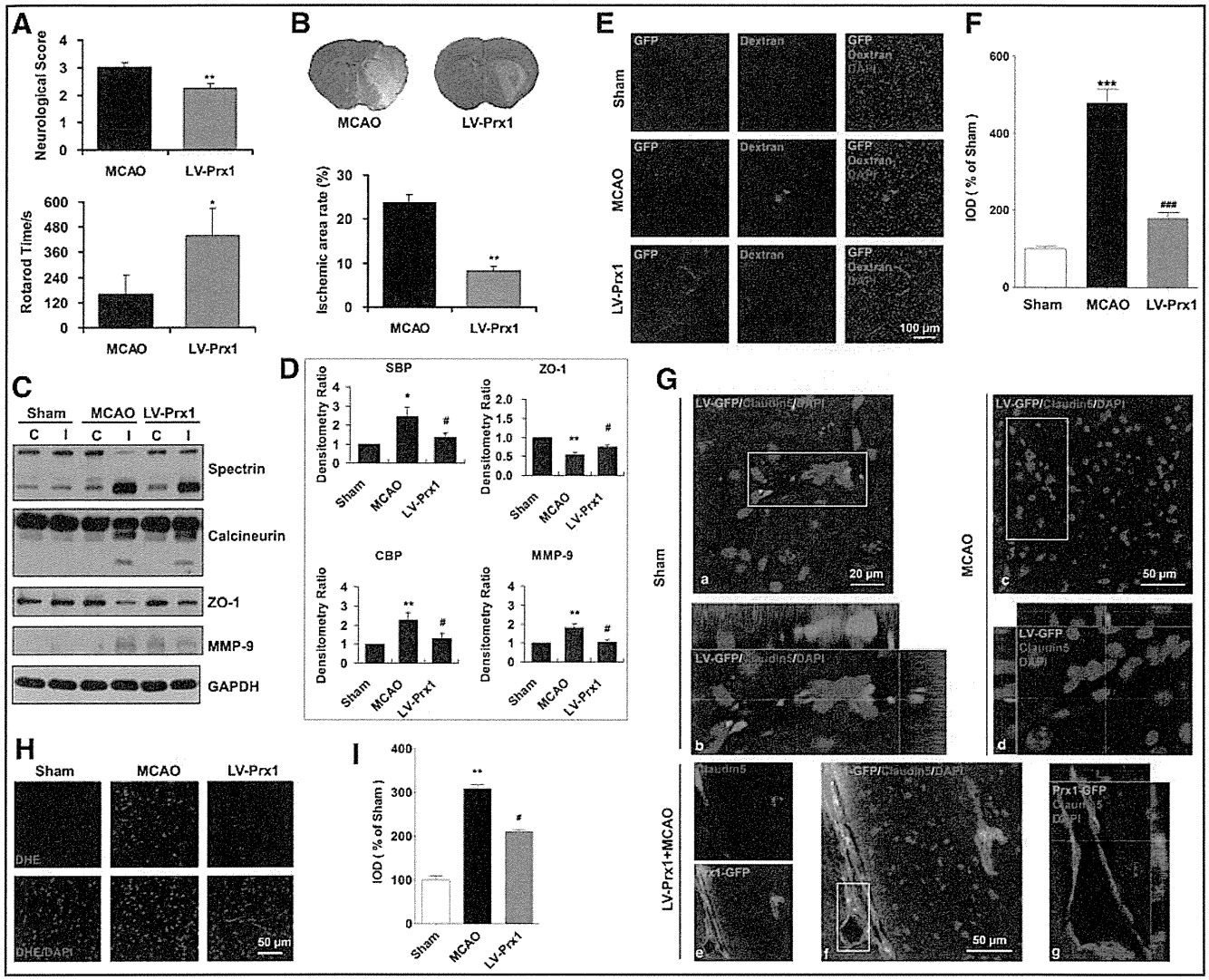


**FIG. 9. Lentiviral-mediated delivery of Prx1 protects against neurovascular protection in tMCAO mice.** **(A)** Lentiviral-mediated delivery of Prx1 improved neurological functional recovery after focal ischemia. The neurological scores (*upper*) and rotarod test (*lower*) were examined. The data are expressed as the percentage of the values observed in vehicle-treated animals (mean ± SEM, $n = 10$). $^{*}p < 0.05$; $^{**}p < 0.01$ *versus* vehicle-treated mice. **(B)** LV-*Prx1* transduction reduced the infarct area of mice 24 h after tMCAO. The mice were subjected to 45 min of MCAO, and the infarct area was quantified 24 h later in cresyl violet-stained brain sections. The data are expressed as the percentage of the infarct area/total area of each brain section (mean ± SEM, $n = 10$). $^{**}p < 0.01$ *versus* vehicle-treated mice. **(C)** The effect of LV-*Prx1* on neurovascular damage after brain ischemia. The proteins from penumbra brain region of mice were immunoblotted with antibodies against spectrin, calcineurin, ZO-1, and MMP-9, which are indicative antibodies for neurovascular damage. C, contralateral; I, ipsilateral. **(D)** The quantitative analyses are shown in the bar graph as the percentage of values of sham-operated animals (mean ± SEM, $n = 4$). $^{*}p < 0.05$; $^{**}p < 0.01$ *versus* sham mice; $^{\#}p < 0.05$ *versus* vehicle-treated mice. Immunoblotting with an anti-$\beta$-actin antibody demonstrated equal protein loading in each lane. SBP, spectrin breakdown products; CBP, calcineurin breakdown products. **(E)** LV-*Prx1* transduction attenuated BBB disruption 24 h after tMCAO. Mice were intravenously injected with Texas red-dextran in saline and perfused 120 min later. *Ex vivo* dextran labeling (red fluorescence) indicated extensive BBB permeability around disrupted brain microvessels in tMCAO mice. **(F)** Quantification of Texas red-dextran immunofluorescence expressed as integrated optical density (IOD). $^{***}p < 0.001$ *versus* sham; $^{\#\#\#}p < 0.001$ *versus* vehicle-treated mice. **(G)** Effect of LV-*Prx1* transduction on the degradation of claudin5. **(a)** Immunostaining with anti-claudin5 (red fluorescence) antibody showed brain ischemia-induced claudin5 degradation **(c, d)** in the microvessels 24 h after tMCAO. LV-*Prx1* transduction reduced the degradation of claudin5 **(e–g)** in the microvessels 24 h after tMCAO. Higher-magnification images of microvessel staining **(b, d, g)** from the *insets* of **(a, c, f)**, respectively. **(H)** The effect of *Prx1* transduction on $O_2^{\bullet -}$ levels, as determined by *in situ* dihydroethidium staining. LV-*Prx1* transduction reduced the $O_2^{\bullet -}$ level in the penumbra region compared to vehicle. Each image shown is representative of five independently injected mice. DHE, dihydroethidium. **(I)** The quantitative analyses of dihydroethidium immunofluorescence are shown in the bar graph. $^{**}p < 0.01$ *versus* sham; $^{\#}p < 0.05$ *versus* vehicle-treated mice. BBB, blood–brain barrier; $O_2^{\bullet -}$, superoxide. To see this illustration in color, the reader is referred to the web version of this article at www.liebertpub.com/ars

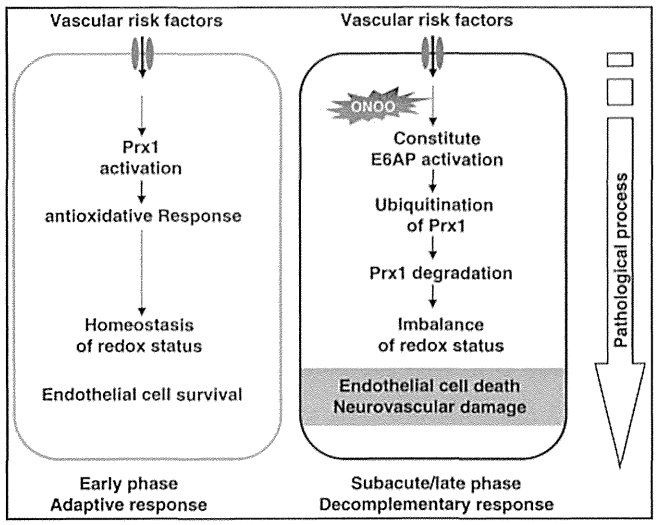


**FIG. 10. Schematic illustration of the mechanisms by which nitrosative stress induces Prx1 ubiquitination in endothelial cells during ischemic insult *via* E6AP activation.** To see this illustration in color, the reader is referred to the web version of this article at www.liebertpub.com/ars

BBB damage, preserved the ZO-1, and prevented the activation of metalloproteinases (MMPs). This is similar to the reports that Prx1 was required also for neurovascular cell survival during exposure to pathogenic proteins associated with brain ischemia or with amyloid-$\beta$ expression in neurons (30). These results are consistent with the finding that *Prx1*-deficient mice suffer embryonic lethality because they lack essential antioxidant function (25, 34, 39). Although the neurovascular cells might be a critical issue during the earlier phase of brain ischemia, the functional coupling and collaborations among the capillaries, glia, and neurons of the brain should be taken into consideration (9, 37). For instance, recent studies highlight that pericyte loss causes BBB breakdown and neurodegeneration (2, 36). Therefore, how Prx1-mediated vascular protection contributed to the neuronal survival in the present study, however, is a topic for further investigation. Prx1 protein levels can prevent excessive ROS accumulation by interaction with thioredoxin to detoxify hydrogen peroxide ($H_2O_2$), $ONOO^-$, and a range of organic hydroperoxides (34). We found further that LV transduction reduced $O_2^{\bullet -}$ formation in the ipsilateral region of the ischemia brain, which might be a consequence of ERK and FKHR activation by Prx1. Indeed, Prxs participate in a very wide range of reactions, including neuronal differentiation, cell signaling, molecular chaperoning, and mitochondrial function, in both catalytic-dependent and catalytic-independent manners and can interact with JNK, c-Abl, and apoptosis signal-regulating kinase 1 (ASK1) in a redox-regulated manner (11, 14, 21, 23). Here, ipsilateral sections showed stronger GFP fluorescence in cerebral vessels of tMCAO mice, it might due to the changes of structural integrity in ischemic region, where dividing cell also largely accumulated (12, 20).

In summary, our studies identify an intracellular link between nitrosative stress and Prx1 signaling in endothelial cells following ischemia-like injury. Our description of an early ischemia-induced activation of beneficial Prx1 generation followed by subsequent inactivation represents a previously undescribed, nitrosative stress-dependent process mediated by E6AP-dependent Prx1 ubiquitination and subsequent endothelial barrier damage. Since Prx1 protected against oxidative stress in endothelial cells to reduce injury after ischemia, both *in vitro*- and *in vivo*-specific inducers of the Prx1 pathway, or mechanisms to prevent its degradation, may be targeted for therapeutic benefit in neurovascular disorders.

## Materials and Methods

### *Reagents*

Dulbecco's modified Eagle's medium (DMEM) and fetal bovine serum were purchased from Gibco. Alexa Fluor 488-conjugated anti-rabbit IgG and Alexa Fluor 594-conjugated anti-mouse IgG were obtained from Invitrogen. Uric acid was obtained from Wako. 5,10,15,20-Tetrakis-[4-sulfonatophenyl]-porphyrinato-iron[III] (FeTPPS; Calbiochem) was used as a specific $ONOO^-$ decomposition catalyst. Unless otherwise stated, all reagents and chemicals were obtained from Sigma-Aldrich.

### *OGD exposure and experimental treatments of cell cultures*

EA.hy926 cells (16, 43), HBMECs, and mouse brain microvascular endothelial cells (bEnd.3) were used for Western blot or immunocytochemistry in the present study. Briefly, in the oxygen and glucose deprivation phase, the culture medium was replaced and washed with glucose-free Hank's balanced salt solution, after which the cultures were placed in an airtight experimental hypoxia chamber (Billups-Rothenberg) containing a gas mixture comprising 95% $N_2$ and 5% $CO_2$. To mimic an ischemia-like condition *in vitro*, cell cultures were exposed to OGD for 1, 3, 6, 12, and 24 h. Cells without OGD served as controls.

### *Two-dimensional gel electrophoresis*

Approximately 450 $\mu$g of protein was resuspended in a rehydration solution [8 *M* Urea, 2% CHAPS, 20 m*M* DTT, 0.2% Biolyte (pH range 3–10), and 0.2% Bromphenol blue] and applied to 17-cm pH 3–10 nonlinear gradient immobiline strips for isoelectric focusing. Isoelectric focusing was performed using Protean IEF Cell (Bio-Rad), and the proteins in the IPG strips were subsequently placed on a 12% uniform sodium dodecyl sulfate (SDS)–polyacrylamide gel. The gels were silver stained and scanned with an Image Scanner in transmission mode, after which image analysis was conducted with two-dimensional PDquest (Bio-Rad). The two-dimensional gel electrophoresis was repeated three times using independently grown cultures.

### *In-gel digestion and mass spectrometry analysis*

The in-gel digestion of proteins for mass spectrometric characterization was performed as published previously (47). After the tryptic peptide mixture was dissolved with 0.5% trifluoroacetic acid, peptide mass analysis was performed using an AB4800 MALDI-TOF/TOF mass spectrometer (Applied Biosystems). The mass spectra were externally calibrated with a peptide standard from Applied Biosystems. Based on the National Center for Biotechnology Information

(NCBI) human databases, the mass spectra were analyzed with a 50 ppm mass tolerance by GPS Explorer version 2.0.1 and Mascot version 1.9.

### *Plasmid constructs and transfections*

The EA.hy926 or HBMEC endothelial cells were cultured in six-well plates in the growth medium and transfected with plasmid DNA encoding *Prx1*, *siPrx1*, *siE6AP*, *pRK5-HA-Ubiquitin-K48R* (17604; Addgene), or an empty plasmid control using Attractene (Qiagen). After transfection for 2 days, the cells were collected for related experiments. To express the active-site cysteine-to-alanine mutant of E6AP in endothelial cells, *p3869HA-E6AP C833A* cells (8649; Addgene) were used. The C-A mutation was introduced at the site of E6AP C833 (22, 27). The *K48R mutant ubiquitin* was obtained from Dr. Guanghui Wang (Soochow University) (27). All the constructs were confirmed by sequencing.

### *Lentiviral vectors preparation for brain delivery*

To construct a lentiviral vector expressing Prx1, two complementary *Prx1* DNA oligonucleotides were synthesized and inserted into the *Eco*RI-*Bam*HI site of transfer vector *pCDH-CMV-MCS-EF1-copGFP* under the control of promoter *CMV*. The constructed vector was transformed into DH5a *Escherichia coli* and isolated with minipreps plasmid purification system (Promega). A large production of LV-*Prx1* was prepared by transfection of human kidney 293T cells. In brief, 293T cells were cotransfected with a mixture containing packaging plasmid (*pCD/NL-BH*DDD*), envelope plasmid (*pLTR-G*), and transfer vector and Trans-EZ. For high-titer virus stocks, the supernatant of cells was collected at 72 h after transfection, low-speed centrifuged, filtered, and ultracentrifuged. The titer of LV-*Prx1* stock was determined by transduction of HOS cells with serial dilutions of concentrated lentivirus and analyzing integrated viral DNA copies per cell by quantitative polymerase chain reaction. The lentiviral vectors coding for *GFP* without *Prx1* were prepared in a similar manner, as described above, and used as a control (LV-*GFP*). In addition, we used a lentivirus-mediated RNA interference approach to achieve the inhibition of E6AP levels in the brain. The short hairpin RNA (shRNA)-mediated *Ube3a* knockdown vectors were constructed by subcloning the U6 promoter-sh-*Ube3a* cassette into the *Age*I-*Eco*RI sites of the *pLenti-CMV* vector.

The lentiviral vector encoding mouse *Prx1* (LV-*GFP-Prx1*), LV-*GFP*, or sh-*E6AP* was injected into the right lateral ventricle over a 10-min duration using a Hamilton microsyringe with the coordinates of 0.5 mm caudal to the bregma, 1 mm lateral to the midline, and 3 mm depth from the skull surface under the guidance of a stereotaxic instrument. Two weeks after the introduction of the viral vectors, the MCAO mice model was prepared as previously reported (51). All lentivirus batches used for experiments had comparable titers ranging from $1\times10^8$ to $1\times10^9$ integration units/ml. Virus suspensions were stored at −80°C until use and were briefly centrifuged and kept on ice immediately before injection.

### *RNA interference*

*Prx1* siRNAs or *E6AP* siRNAs was introduced into EA.hy926 cells with the transfection medium according to the manufacturer's instructions. The control set of EA.hy926 cells was transfected with nontargeted siRNAs. The cells were collected for experiments 72 h after transfection. Knockdown was confirmed with Western blotting using whole cell lysates. si*Prx1* (sc-36177) and scramble negative control (sc-37007) were obtained from Santa Cruz Biotechnology: si*E6AP* (sense), 5′-GCCCAGACACAGAA AGGUUTT-3′; scramble negative control (siCont-1, sense), 5′-UUGCGGGUCUAAUCACCGATT-3′.

### *Annexin V/PI flow cytometry analysis*

Flow cytometric assays to evaluate apoptosis by Annexin V/PI (BioVision) staining were performed essentially as previously described, following the manufacturer's instruction. Briefly, endothelial cells were transfected with *Prx1* siRNAs for 48 h before exposure to 6 h OGD. Annexin V-FITC and PI were added to the cell suspension and incubated at room temperature for 10 min in the dark. For each sample, at least $1\times10^4$ cells were analyzed using a FACS-Calibur flow cytometer (BD Biosciences).

### *TUNEL assay*

*In situ* DNA fragmentation was assessed using a TUNEL staining combined with 4′,6-diamidino-2-phenylindole (DAPI) counterstain. Images were recorded after counterstaining with DAPI (nuclei marker), and endothelial cells were identified by phase image. Endothelial cells were imaged using 20× objectives. The apoptotic response was expressed as the percentage of TUNEL-positive endothelial cells/the total number of nuclei counted after DAPI staining. The results represented the average of a minimum of three experiments, and a minimum of 600 cells were counted per experiment.

### *Cell fractionation, immunoprecipitation, and immunoblotting analysis*

Immunoblotting was carried out in endothelial cell lysates after determination of protein concentrations using the Bradford's solution. The cell lysates containing equivalent amounts of protein were applied to 10%–13.5% acrylamide denaturing gels (SDS-polyacrylamide gel electrophoresis [PAGE]) (15). Proteins were then transferred to an immobilon polyvinylidene difluoride membrane for 1 h at 50 V. Membranes were blocked in 20 m*M* Tris-HCl (PH 7.4), 150 m*M* NaCl, and 0.1% Tween 20 (TBS-T) containing 5% fat-free milk powder for 1 h and immunodetected with antibodies to HSP27 monoclonal antibody (1:1000), Prx1 polyclonal antibody (1:5000), (Abcam); HO-1 (1:1000), Phospho-AKT (1:1000), Phospho-ERK (1:3000), Phospho-JNK (1:1000), Phospho-P38 (1:1000), Phospho-FKHR (1:3000), and cleaved Caspase-3 (1:1000, polyclonal antibody; Cell Signaling Technology); procaspase-3 (1:2000), PARP-1 (1:2000), and ubiquitin (1:1000, polyclonal antibody; Santa Cruz Biotechnology); ZO-1 and Occludin (1:1000; Invitrogen); E6AP (1:3000) and β-actin (1:5000, monoclonal antibody; Sigma-Aldrich). After incubation for 12 h, membranes were incubated with the appropriate horseradish peroxidase-conjugated secondary antibody. Immunoreactivity was visualized by enhanced chemiluminescence (Amersham Life Science). The Prx1 ubiquitylation assays were performed essentially as described previously (46). Briefly, cells were treated with 5 μ*M* MG132 (Calbiochem)

or with dimethyl sulfoxide (DMSO; control) for 30 min before OGD. Immunoprecipitates were analyzed by immunoblotting, using either anti-ubiquitin or anti-Prx1 antibody to detect ubiquitylated Prx1. In addition, E6AP immunoprecipitates from the lysates were probed with anti-nitrotyrosine antibody.

### *Experimental animals*

Male C57 mice, weighing 20–23 g, were obtained from the Zhejiang Medical Animal Centre (Hangzhou, China). Mice were housed under climate-controlled conditions with a 12-h light/dark cycle and provided with standard food and water. Animals were acclimated to their environment for at least 1 week before initiating the experimental protocols. All experimental protocols and animal handling procedures were performed in accordance with the National Institutes of Health (NIH) guidelines for the care and use of laboratory animals and were approved by the Committee for Animal Experiments at the Zhejiang University in China.

### *tMCAO model*

The transient/reperfusion MCAO model was used to resemble stroke in humans (3, 5), and the surgery was carried out as previously described (18). Animal procedures were approved by the Committee on Animal Experiments at the Zhejiang University. The rectal temperature was monitored throughout the surgery, and the body temperature was maintained at 37°C ± 0.5°C with a heating pad. Neurological deficit tests were carried out at 24 h after tMCAO, including neurological scores and rotarod test. Neurological scores were determined 24 h after tMCAO using a previously described scoring system (45). Rotarod test, which started 3 days before the surgery to train five times every day, was performed to examine the motor coordination. The rotarod time (s) that mice persisted on the rotarod after ischemia was recorded; the data were expressed as the mean duration of five trials at 24 h after tMCAO. The brain infarct area of mice 24 h after ischemia was evaluated from scanned digital images of Nissl-stained brain sections using Image J software (NIH).

### *Evaluation of BBB damage*

The loss of BBB integrity was also verified by the leakage of Texas red-conjugated dextran from microvessels after intravenous injection. Texas red-dextran (70 kDa) solution (0.1% in phosphate-buffered saline [PBS], 5 ml/kg) was intravenously administered *via* the tail vein at 22 h after the onset of MCAO. The mice were perfused transcardially with saline as above. After decapitation, brains were prepared according to the immunohistochemical methods, and Texas red-dextran leakage was determined by immunofluorescence staining (red fluorescence).

### *Confocal immunofluorescence staining and analysis*

For immunofluorescence analysis in cultured endothelial cells, cells were fixed in 4% formaldehyde/PBS as previously reported (16). Cells were labeled with Prx1 (1:300, polyclonal antibody; Abcam), Nitrotyrosine (1:200, monoclonal antibody; Millipore), E6AP (1:300, polyclonal antibody; Invitrogen), and ubiquitin (1:200, monoclonal antibody; Cell Signaling Technology), followed by immunofluorescence using a standard protocol from PerkinElmer Life Sciences, Inc. Nuclei were stained with DAPI dihydrochloride bisbenzimide (5 $\mu M$). Immunolocalization and changes in Prx1, E6AP, and nitrotyrosine in cultured endothelial cells were visualized by confocal microscopy (Zeiss LSM 510).

For immunohistochemistry, mice were anesthetized at the time of sacrifice and transcardially perfused with 4% paraformaldehyde in PBS as previously described (16). The whole brains were immediately removed and post-fixed overnight at 4°C. Then, brains were cut into 35-$\mu$m-thick serial sections using a vibratome. Sections were incubated at room temperature in PBS with 0.01% Triton-X100 for 30 min and for 1 h in 3% bovine serum albumin (BSA) in PBS. For immunolabeling, the brain slices were incubated with antibodies targeting Prx1 (1:300; Abcam), CD31 (1:200; Santa Cruz Biotechnology), Claudin5 (1:200; Invitrogen), E6AP (1:300; Sigma-Aldrich), NeuN (1:300), and Nitrotyrosine (1:200) (Millipore) overnight at 4°C. After washing, the sections were incubated with Alexa fluor 488-conjugated anti-rabbit IgG (1:400) and Alexa fluor 594-conjugated anti-mouse IgG (1:400) (Invitrogen) in (Tris-NaCl-blocking) TNB buffer (1:400). In addition, the oxidative fluorescent indicator dihydroethidium was used to evaluate *in situ* $O_2^{\bullet -}$ generation as previously reported (45). Immunofluorescence was visualized by using a Zeiss LSM 510 confocal microscope.

### *Statistical analysis*

The data were analyzed with *t*-tests when means between two groups were compared. For multigroup comparisons, statistical significance was determined using one-way ANOVA followed by a *post hoc* Tukey's test or Dunnett's comparison to control. All data are expressed as the mean ± SEM. A value of $p < 0.05$ was considered to be significant.

## Acknowledgments

This work was supported in part by the National Natural Science Foundation of China (81120108023, 91232705, 81202533); the Zhejiang Provincial Qianjiang Talent Plan (2012R10036); the Zhejiang Provincial Natural Science Foundation of China (R2100281); NIH grants (NHLBI HL-68686, NIDDK DK-49870, and DK-36079).

## Author Disclosure Statement

No competing financial interests exist.

## References

1. Aracena P, Tang W, Hamilton SL, and Hidalgo C. Effects of S-glutathionylation and S-nitrosylation on calmodulin binding to triads and FKBP12 binding to type 1 calcium release channels. *Antioxid Redox Signal* 7: 870–881, 2005.
2. Armulik A, Genové G, Mäe M, Nisancioglu MH, Wallgard E, Niaudet C, He L, Norlin J, Lindblom P, Strittmatter K, Johansson BR, and Betsholtz C. Pericytes regulate the blood-brain barrier. *Nature* 468: 557–561, 2010.
3. Braeuninger S and Kleinschnitz C. Rodent models of focal cerebral ischemia: procedural pitfalls and translational problems. *Exp Transl Stroke Med* 1: 8, 2009.
4. Brunet Simioni M, De Thonel A, Hammann A, Joly AL, Bossis G, Fourmaux E, Bouchot A, Landry J, Piechaczyk M, and Garrido C. Heat shock protein 27 is involved in SUMO-2/3 modification of heat shock factor 1 and thereby

modulates the transcription factor activity. *Oncogene* 28: 3332–3344, 2009.
5. Carmichael ST. Rodent models of focal stroke: size, mechanism, and purpose. *NeuroRx* 2: 396–409, 2005.
6. Chae HZ, Kang SW, and Rhee SG. Isoforms of mammalian peroxiredoxin that reduce peroxides in presence of thioredoxin. *Methods Enzymol* 300: 219–226, 1999.
7. Chae HZ, Oubrahim H, Park JW, Rhee SG, and Chock PB. Protein glutathionylation in the regulation of peroxiredoxins: a family of thiol-specific peroxidases that function as antioxidants, molecular chaperones, and signal modulators. *Antioxid Redox Signal* 16: 506–523, 2012.
8. Coe H, Bedard K, Groenendyk J, Jung J, and Michalak M. Endoplasmic reticulum stress in the absence of calnexin. *Cell Stress Chaperones* 13: 497–507, 2008.
9. del Zoppo GJ. . The neurovascular unit, matrix proteases, and innate inflammation. *Ann N Y Acad Sci* 1207: 46–49, 2010.
10. Fisher AB. Peroxiredoxin 6: a bifunctional enzyme with glutathione peroxidase and phospholipase $A_2$ activities. *Antioxid Redox Signal* 15: 831–844, 2011.
11. Gan Y, Ji X, Hu X, Luo Y, Zhang L, Li P, Liu X, Yan F, Vosler P, Gao Y, Stetler RA, and Chen J. Transgenic overexpression of peroxiredoxin-2 attenuates ischemic neuronal injury *via* suppression of a redox-sensitive pro-death signaling pathway. *Antioxid Redox Signal* 17: 719–732, 2012.
12. Geraerts M, Eggermont K, Hernandez-Acosta P, Garcia-Verdugo JM, Baekelandt V, and Debyser Z. Lentiviral vectors mediate efficient and stable gene transfer in adult neural stem cells *in vivo*. *Hum Gene Ther* 17: 635–650, 2006.
13. Girouard H, Park L, Anrather J, Zhou P, and Iadecola C. Cerebrovascular nitrosative stress mediates neurovascular and endothelial dysfunction induced by angiotensin II. *Arterioscler Thromb Vasc Biol* 27: 303–309, 2007.
14. Guo X, Yamada S, Tanimoto A, Ding Y, Wang KY, Shimajiri S, Murata Y, Kimura S, Tasaki T, Nabeshima A, Watanabe T, Kohno K, and Sasaguri Y. Overexpression of peroxiredoxin 4 attenuates atherosclerosis in apolipoprotein E knockout mice. *Antioxid Redox Signal* 17: 1362–1375, 2012.
15. Han F, Ali Raie A, Shioda N, Qin ZH, and Fukunaga K. Accumulation of beta-amyloid in the brain microvessels accompanies increased hyperphosphorylated tau proteins following microsphere embolism in aged rats. *Neuroscience* 153: 414–427, 2008.
16. Han F, Chen YX, Lu YM, Huang JY, Zhang GS, Tao RR, Ji YL, Liao MH, Fukunaga K, and Qin ZH. Regulation of the ischemia-induced autophagy-lysosome processes by nitrosative stress in endothelial cells. *J Pineal Res* 51: 124–135, 2011.
17. Han F, Shirasaki Y, and Fukunaga K. Microsphere embolism-induced endothelial nitric oxide synthase expression mediates disruption of the blood-brain barrier in rat brain. *J Neurochem* 99: 97–106, 2006.
18. Han F, Tao RR, Zhang GS, Lu YM, Liu LL, Chen YX, Lou YJ, Fukunaga K, and Hong ZH. Melatonin ameliorates ischemic-like injury-evoked nitrosative stress: Involvement of HtrA2/PED pathways in endothelial cells. *J Pineal Res* 50: 281–291, 2011.
19. Hu BR, Martone ME, Jones YZ, and Liu CL. Protein aggregation following transient cerebral ischemia. *J Neurosci* 20: 3191–3199, 2000.
20. Jakobsson J and Lundberg C. Lentiviral vectors for use in the central nervous system. *Mol The* 13: 484–493, 2006.
21. Kakihana T, Nagata K, and Sitia R. Peroxides and peroxidases in the endoplasmic reticulum: integrating redox homeostasis and oxidative folding. *Antioxid Redox Signal* 16: 763–771, 2012.
22. Kao WH, Beaudenon SL, Talis AL, Huibregtse JM, and Howley PM. Human papillomavirus type 16 E6 induces self-ubiquitination of the E6AP ubiquitin-protein ligase. *J Virol* 74: 6408–6417, 2000.
23. Kim SY, Kim TJ, and Lee KY. A novel function of peroxiredoxin 1 (Prx-1) in apoptosis signal-regulating kinase 1 (ASK1)-mediated signaling pathway. *FEBS Lett* 582: 1913–1918, 2008.
24. Kim YJ, Ahn JY, Liang P, Ip C, Zhang Y, and Park YM. Human prx1 gene is a target of Nrf2 and is upregulated by hypoxia/reoxygenation: implication to tumor biology. *Cancer Res* 67: 546–554, 2007.
25. Kisucka J, Chauhan AK, Patten IS, Yesilaltay A, Neumann C, Van Etten RA, Krieger M, and Wagner DD. Peroxiredoxin1 prevents excessive endothelial activation and early atherosclerosis. *Circ Res* 103: 598–605, 2008.
26. Leblanc GG, Golanov E, Awad IA, and Young WL. Biology of Vascular Malformations of the Brain NINDS Workshop Collaborators. Biology of vascular malformations of the brain. *Stroke* 40: e694–e702, 2009.
27. Liu C, Fei E, Wang H, Tao R, Iwata A, Nukina N, Zhou J, and Wang G. Assembly of lysine 63-linked ubiquitin conjugates by phosphorylated-synuclein implies lewy body biogenesis. *J Biol Chem* 282: 14558–14566, 2007.
28. Liu G, Feinstein SI, Wang Y, Dodia C, Fisher D, Yu K, Ho YS, and Fisher AB. Comparison of glutathione peroxidase 1 and peroxiredoxin 6 in protection against oxidative stress in the mouse lung. *Free Radic Biol Med* 49: 1172–1181, 2010.
29. Liu QB, Liu LL, Lu YM, Tao RR, Huang JY, Han F, and Lou YJ. The induction of reactive oxygen species and loss of mitochondrial Omi/HtrA2 is associated with S-nitrosoglutathione-induced apoptosis in human endothelial cells. *Toxicol Appl Pharmacol* 244: 374–384, 2010.
30. Manczak M, Mao P, Calkins MJ, Cornea A, Reddy AP, Murphy MP, Szeto HH, Park B, and Reddy PH. Mitochondria-targeted antioxidants protect against amyloid-beta toxicity in Alzheimer's disease neurons. *J Alzheimers Dis* 20: S609–S631, 2010.
31. Mowbray AL, Kang DH, Rhee SG, Kang SW, and Jo H. Laminar shear stress up-regulates peroxiredoxins (PRX) in endothelial cells: PRX 1 as a mechanosensitive antioxidant. *J Biol Chem* 283: 1622–1627, 2008.
32. Nakamura T and Lipton SA. S-nitrosylation of critical protein thiols mediates protein misfolding and mitochondrial dysfunction in neurodegenerative diseases. *Antioxid Redox Signal* 14: 1479–1492, 2011.
33. Nasu J, Murakami K, Miyagawa S, Yamashita R, Ichimura T, Wakita T, Hotta H, Miyamura T, Suzuki T, Satoh T, and Shoji I. E6AP ubiquitin ligase mediates ubiquitin-dependent degradation of peroxiredoxin 1. *J Cell Biochem* 111: 676–685, 2010.
34. Neumann CA, Krause DS, Carman CV, Das S, Dubey DP, Abraham JL, Bronson RT, Fujiwara Y, Orkin SH, and Van Etten RA. Essential role for the peroxiredoxin Prdx1 in erythrocyte antioxidant defence and tumour suppression. *Nature* 424: 561–565, 2003.
35. Pitts A, Dailey K, Newington JT, Chien A, Arseneault R, Cann T, Thompson LM, and Cumming RC. Dithiol based compounds maintain expression of antioxidant protein

peroxiredoxin 1 that counteracts toxicity of mutant hungtington. *J Biol Chem* 287: 22717–22729, 2012.
36. Quaegebeur A, Segura I, and Carmeliet P. Pericytes: blood-brain barrier safeguards against neurodegeneration? *Neuron* 68: 321–323, 2010.
37. Quaegebeur A, Lange C, and Carmeliet P. The neurovascular link in health and disease: molecular mechanisms and therapeutic implications. *Neuron* 71: 406–424, 2011.
38. Rabilloud T, Heller M, Gasnier F, Luche S, Rey C, Aebersold R, Benahmed M, Louisot P, and Lunardi J. Proteomics analysis of cellular response to oxidative stress. Evidence for *in vivo* overoxidation of peroxiredoxins at their active site. *J Biol Chem* 277: 19396–19401, 2002.
39. Rani V, Neumann CA, Shao C, and Tischfield JA. Prdx1 deficiency in mice promotes tissue specific loss of heterozygosity mediated by deficiency in DNA repair and increased oxidative stress. *Mutat Res* 735: 39–45, 2012.
40. Riddell JR, Maier P, Sass SN, Moser MT, Foster BA, and Gollnick SO. Peroxiredoxin 1 stimulates endothelial cell expression of VEGF *via* TLR4 dependent activation of HIF-1α. *PLoS One* 7: e50394, 2012.
41. Rizzo MT and Leaver HA. Brain endothelial cell death: modes, signaling pathways, and relevance to neural development, homeostasis, and disease. *Mol Neurobiol* 42: 52–63, 2010.
42. Rott R, Szargel R, Haskin J, Bandopadhyay R, Lees AJ, Shani V, and Engelender S. α-Synuclein fate is determined by USP9X-regulated monoubiquitination. *Proc Natl Acad Sci U S A* 108: 18666–186671, 2011.
43. Satoh M, Fujimoto S, Haruna Y, Arakawa S, Horike H, Komai N, Sasaki T, Tsujioka K, Makino H, and Kashihara N. NAD (P) h oxidase and uncoupled nitric oxide syntase are major sources of glomerular superoxide in rats with experimental diabetic nephropathy. *Am J Physiol Renal Physiol* 288: F1144–F1152, 2005.
44. Schreibelt G, van Horssen J, Haseloff RF, Reijerkerk A, van der Pol SM, Nieuwenhuizen O, Krause E, Blasig IE, Dijkstra CD, Ronken E, and de Vries HE. Protective effects of peroxiredoxin-1 at the injured blood-brain barrier. *Free Radic Biol Med* 45: 256–264, 2008.
45. Shioda N, Han F, Moriguchi S, and Fukunaga K. Constitutively active calcineurin mediates delayed neuronal death through Fas-ligand expression *via* activation of NFAT and FKHR transcriptional activities in mouse brain ischemia. *J Neurochem* 102: 1506–1517, 2007.
46. Shirakura M, Murakami K, Ichimura T, Suzuki R, Shimoji T, Fukuda K, Abe K, Sato S, Fukasawa M, Yamakawa Y, Nishijima M, Moriishi K, Matsuura Y, Wakita T, Suzuki T, Howley PM, Miyamura T, and Shoji I. E6AP ubiquitin ligase mediates ubiquitylation and degradation of hepatitis C virus core protein. *J Virol* 81: 1174–1185, 2007.
47. Sultana R, Perluigi M, Newman SF, Pierce WM, Cini C, Coccia R, and Butterfield DA. Redox proteomic analysis of carbonylated brain proteins in mild cognitive impairment and early Alzheimer's disease. *Antioxid Redox Signal* 12: 327–336, 2010.
48. Tan KH, Harrington S, Purcell WM, and Hurst RD. Peroxinitrite mediates nitric oxide-induced blood-brain barrier damage. *Neurochem Res* 29: 579–587, 2004.
49. Tao RR, Ji YL, Lu YM, Fukunaga K, and Han F. Targeting nitrosative stress for neurovascular protection: new implications in brain diseases. *Curr Drug Targets* 13: 272–284, 2012.
50. Wilcox CS and Pearlman A. Chemistry and antihypertensive effects of tempol and other nitroxides. *Pharmacol Rev* 60: 418–469, 2008.
51. Zhang GS, Tian Y, Huang JY, Tao RR, Liao MH, Lu YM, Ye WF, Wang R, Fukunaga K, Lou YJ, and Han F. The γ-Secretase blocker DAPT reduces the permeability of the blood-brain barrier by decreasing the ubiquitination and degradation of occludin during permanent brain ischemia. *CNS Neurosci Ther* 19: 53–60, 2012.

Address correspondence to:
*Dr. Feng Han*
*Institute of Pharmacology, Toxicology and Biochemical Pharmaceutics*
*Zhejiang University*
*Hangzhou 310058*
*China*

*E-mail:* changhuahan@zju.edu.cn

Date of first submission to ARS Central, April 18, 2013; date of final revised submission, November 12, 2013; date of acceptance, December 2, 2013.

**Abbreviations Used**

ASK1 = apoptosis signal-regulating kinase 1
BBB = blood–brain barrier
DAPI = 4′,6-diamidino-2-phenylindole
DMEM = Dulbecco's modified Eagle's medium
E6AP = E6-associated protein
ER = endoplasmic reticulum
FKHR = forkhead transcription factor Foxo1
$H_2O_2$ = hydrogen peroxide
HBMEC = human brain microvascular endothelial cell
HO-1 = heme oxygenase-1
HSP27 = heat shock protein 27
JNK = c-Jun N-terminal kinase
MALDI-TOF = matrix-assisted laser desorption/ionization-time-of-flight
mHtt = mutant Hungtington
MMPs = metalloproteinases
NeuN = neuronal nuclear marker
NO = nitric oxide
Nrf2 = NF-E2-related factor 2
$O_2^{\bullet-}$ = superoxide
OGD = oxygen–glucose deprivation
$ONOO^-$ = peroxynitrite
PAGE = polyacrylamide gel electrophoresis
PARP = poly ADP-ribose polymerase
PBS = phosphate-buffered saline
PI = propidium iodide
Prx = peroxiredoxin
ROS = reactive oxygen species
SDS = sodium dodecyl sulfate
shRNA = short hairpin RNA
SIN-1 = 3-morpholinosydnonimine
siRNA = small interfering RNA
tMCAO = transient middle cerebral artery occlusion
TUNEL = terminal deoxynucleotidyl transferase dUTP nick end labeling
ZO-1 = zonula occludens-1

Toxicology and Applied Pharmacology 282 (2015) 237–243

Contents lists available at ScienceDirect

Toxicology and Applied Pharmacology

journal homepage: www.elsevier.com/locate/ytaap

# Mitochondrial iron accumulation exacerbates hepatic toxicity caused by hepatitis C virus core protein

Shuichi Sekine [a], Konomi Ito [a], Haruna Watanabe [a], Takafumi Nakano [a], Kyoji Moriya [b], Yoshizumi Shintani [b], Hajime Fujie [b], Takeya Tsutsumi [b], Hideyuki Miyoshi [b], Hidetake Fujinaga [b], Seiko Shinzawa [b], Kazuhiko Koike [b], Toshiharu Horie [a,*]

[a] Laboratory of Biopharmaceutics, Graduate School of Pharmaceutical Sciences, Chiba University, 1-8-1 Inohana, Chuo-ku, Chiba 260-8675, Japan
[b] Department of Internal Medicine, Graduate School of Medicine, The University of Tokyo, 7-3-1 Hongo, Bunkyo-ku, Tokyo 113-8655, Japan

ARTICLE INFO

*Article history:*
Received 8 September 2014
Revised 9 December 2014
Accepted 16 December 2014
Available online 27 December 2014

*Keywords:*
$Ca^{2+}$ uniporter
Fenton reaction
Reactive oxygen species
Ru360
Hepatitis C virus

ABSTRACT

Patients with long-lasting hepatitis C virus (HCV) infection are at major risk of hepatocellular carcinoma (HCC). Iron accumulation in the livers of these patients is thought to exacerbate conditions of oxidative stress. Transgenic mice that express the HCV core protein develop HCC after the steatosis stage and produce an excess of hepatic reactive oxygen species (ROS). The overproduction of ROS in the liver is the net result of HCV core protein-induced dysfunction of the mitochondrial respiratory chain. This study examined the impact of ferric nitrilacetic acid (Fe-NTA)-mediated iron overload on mitochondrial damage and ROS production in HCV core protein-expressing HepG2 (human HCC) cells (Hep39b cells). A decrease in mitochondrial membrane potential and ROS production were observed following Fe-NTA treatment. After continuous exposure to Fe-NTA for six days, cell toxicity was observed in Hep39b cells, but not in mock (vector-transfected) HepG2 cells. Moreover, mitochondrial iron ($^{59}Fe$) uptake was increased in the livers of HCV core protein-expressing transgenic mice. This increase in mitochondrial iron uptake was inhibited by Ru360, a mitochondrial $Ca^{2+}$ uniporter inhibitor. Furthermore, the Fe-NTA-induced augmentation of mitochondrial dysfunction, ROS production, and cell toxicity were also inhibited by Ru360 in Hep39b cells. Taken together, these results indicate that $Ca^{2+}$ uniporter-mediated mitochondrial accumulation of iron exacerbates hepatocyte toxicity caused by the HCV core protein.


## Introduction

Hepatitis C virus (HCV) infection is a major cause of chronic liver disease. About 120–200 million people are infected with HCV, increasing their risk of developing chronic hepatitis, cirrhosis, and eventually hepatocellular carcinoma (HCC) (Ikeda et al., 1998; Nishioka et al., 1991). The HCV genome is approximately 9.6 kb in size and encodes a polyprotein of ~3000 amino acids. The large HCV polyprotein is cleaved by host and viral proteases to generate at least ten smaller proteins, including four structural proteins (one core protein, two envelope proteins, and the E1, E2, and p7 ion channels) (Bukh et al., 1995) and six non-structural proteins (NH2-NS2, NS3, NS4A, NS4B, NS5A, and NS5B-COOH) (Bartenschlager and Lohmann, 2000). These proteins participate in viral replication and also influence cellular functions of the host.

Oxidative stress is commonly observed following HCV infection and is caused by increased levels of cellular reactive oxygen species (ROS) or by changes in cellular antioxidant capacities (Choi and Ou, 2006; Oberley, 2002; Otani et al., 2005). In particular, HCV core protein is known to be closely associated with the mitochondria and causes the increase in host ROS production, lipid peroxidation (Lau et al., 1998; Moriya et al., 2001; Okuda et al., 2002) and mitochondrial $Ca^{2+}$ uptake. HCV core protein also reduces GSH and NADPH concentrations and mitochondrial complex I activities. These undertakings ultimately disrupt mitochondrial membrane permeability and trigger mitochondrial dysfunction (Wang et al., 2010; Wang and Weinman, 2006). As mitochondrial function is the master regulator of cellular energy and apoptotic cell death, mitochondrial injury can culminate in metabolic deficits and steatohepatitis, further exacerbating cell injury and dysfunction.

Due to the relationship between chronic HCV infection and the development of HCC, numerous studies have attempted to identify the HCV proteins that are responsible for hepatocarcinogenesis. These studies indicate that the HCV core protein can promote the immortalization of primary human hepatocytes (Ray et al., 2000), whereas the non-

*Abbreviations:* HCV, hepatitis C virus; HCC, hepatocellular carcinoma; ROS, reactive oxygen species; Fe-NTA, ferric nitrilacetic acid; JC-1, 5,5′,6,6′-tetrachrolo-1,1′,3,3′-tetraethylbenzimidazoly-carbocyanine iodide; CCCP, carbonyl cyanide-m-chlorophenyl hydrazine; MTT, 3-(4,5-dimethylthiazol-2-yl)-2,5-diphenyltetrazolium bromide; HPF, hydroxyphenyl fluorescein; ANT, adenine nucleotide translocator; HRP, horseradish peroxidase; DMEM, Dulbecco's Modified Eagle's Medium; CL, chemiluminescence; TTBS, Tris-buffered saline/0.05% Tween 20; BSA, bovine serum albumin; Hep39b, HCV core protein-expressing HepG2; Hepswx, vector-transfected HepG2.

* Corresponding author at: Faculty of Pharmaceutical Sciences, Teikyo Heisei University, 4-21-2 Nakano, Nakano-ku, Tokyo 164-8530, Japan. Fax: +81 3 5860 4237.
*E-mail address:* t.horie@thu.ac.jp (T. Horie).

http://dx.doi.org/10.1016/j.taap.2014.12.004
0041-008X/

structural proteins NS3 and NS4B can transform NIH 3T3 cells, either individually or in combination with Ha-ras (Park et al., 2000). Iron overload in the liver, which is associated with the genetic disorder hereditary hemochromatosis, has been thought to increase the risk of HCC by about 200-fold (Bonkovsky et al., 1997; Kowdley, 2004). For example, the livers of patients afflicted with HCV are characterized by the elevated expression of transferrin receptor 1 and hepcidin, both of which stimulate iron uptake into hepatocytes (Bonkovsky et al., 1997; Hayashi et al., 1994). In contrast, iron depletion (in the form of dietary iron restriction and/or phlebotomy) can improve hepatic inflammation and lower serum aminotransferase activity in HCV patients (Hayashi et al., 1994). Thus, a major precipitating factor for the pathogenesis of HCV-related liver disease has been attributed to the augmentation of oxidative stress following iron accumulation. However, no underlying cellular mechanism has yet been elucidated.

This study investigated the effect of iron exposure on mitochondrial dysfunction, ROS production and cell toxicity in human hepatoma cells stably expressing the HCV core protein (Hep39b cells). The underlying mechanism responsible for mitochondrial iron accumulation in Hep39b cells and in the livers of HCV core protein-expressing transgenic mice was also examined.

## Materials and methods

*Chemicals and reagents.* Ferric nitrate nonahydrate, nitrilotriacetic acid (NTA), 5,5′,6,6′-tetrachrolo-1,1′,3,3′-tetraethylbenzimidazolycarbocyanine iodide (JC-1), carbonyl cyanide-m-chlorophenyl hydrazine (CCCP) and G418 disulfate were from Sigma Aldrich (St. Louis, MO). MitoTracker® Red was from Invitrogen (Carlsbad, CA). $^{59}FeSO_4$ was from Perkin-Elmer (Waltham, MA). Ru360 was from Merck Millipore Japan (Tokyo, Japan). MTT [3-(4,5-dimethylthiazol-2-yl)-2,5-diphenyltetrazolium bromide] was from Wako Pure Chemical Industries, Ltd. (Osaka, Japan). Hydroxyphenyl fluorescein (HPF) was from Sekisui Medical Co., Ltd. (Tokyo, Japan). Adenine nucleotide translocator (ANT) goat polyclonal IgG, CCDC109A goat polyclonal IgG and horseradish peroxidase (HRP)-conjugated anti-goat IgG were from Santa Cruz Biotechnology, Inc. (Santa Cruz, CA). All chemicals and solvents were of analytical grade.

*Preparation of Fe-NTA.* The Fe-NTA complex was prepared as described by Awai et al. (1979). Briefly, ferric nitrate was dissolved in 1 N HCl to form a 50 mM solution, and NTA was dissolved in 1 N NaOH to form a 150 mM solution. Equal volumes of the two solutions were mixed just before the experiment, and the pH was adjusted to 7.4 with $NaHCO_3$.

*Assessment of cytotoxicity.* Cytotoxicity was assessed by the MTT assay. Briefly, Hep39b and Hepswx cells were seeded into 96 well culture plates at a density of $8.4 \times 10^3$ cells/well and were exposed to various concentrations of Fe-NTA the following day, the medium was replaced with fresh medium containing the same component every 24 h. In some conditions, cells were treated with 20 μM Ru360, a mitochondrial $Ca^{2+}$ uniporter inhibitor, for 1 h prior to Fe-NTA exposure. After six days, the cell culture medium was replaced by 50 μl MTT solution (5 mg/ml MTT in phenol red-free Dulbecco's Modified Eagle's Medium (DMEM)), and the cells were incubated for 2 h at 37 °C. To dissolve the reduced MTT crystals, 200 μl isopropanol was added. The absorbance of the dye was measured at a wavelength of 570 nm, and the turbidity of the cells (background absorbance) was measured at a reference wavelength of 630 nm. The absorbance of the controls (Hepswx and Hep39b) was set at 100%, and cytotoxicity was calculated as the absorbance of the experimental sample relative to that of the control.

*Assessment of ROS production.* ROS production was first assessed by chemiluminescence (CL) analysis. Briefly, cells were seeded into 35 mm glass-bottomed dishes at a density of $2.5 \times 10^5$ cells/dish and exposed to 300 μM Fe-NTA the following day, the medium was replaced with fresh medium containing the same component every 24 h. In some cases, cells were treated with Ru360 for 1 h prior to Fe-NTA treatment. After five days, the cell culture medium was replaced with phenol red-free DMEM containing Fe-NTA and Ru360, and the dish was protected from light. The following day, spontaneous CL was measured using a single photoelectron counting system (CLD-10; Tohoku Electronic Industrial Co., Ltd., Sendai, Japan), as described previously (Maeda et al., 2010). Emission was expressed in counts/10 min/mg protein.

ROS production was also assessed using HPF as a fluorescent probe for the selective detection of hydroxyl radicals. Briefly, cells were seeded into 35 mm glass-bottomed dishes, as described for CL analysis. After 7 days, the cell culture medium was replaced with modified Hanks' balanced salt solution (HBSS) containing 10 mM HEPES, 1 mM $MgCl_2$, 2 mM $CaCl_2$ and 2.7 mM glucose (pH 7.4). Next, 10 μM HPF and 20 nM MitoTracker® Red (a fluorescent probe for the mitochondria) were added, and cells were incubated for 15 min at 37 °C. Images of HPF and MitoTracker® Red staining were obtained using a laser scanning confocal microscope (FV300; Olympus Optical Co., Ltd., Tokyo, Japan). The wavelengths (excitation/emission) for the detection of HPF (green) and MitoTracker® Red (red) were 488 nm/515 nm and 579 nm/599 nm, respectively.

*Assessment of mitochondrial membrane potential.* Measurement of mitochondrial membrane potential was performed using the JC-1 stain, a lipophilic cation fluorescent dye that accumulates in the mitochondria. At a low mitochondrial membrane potential, the JC-1 dye exists as a monomeric molecule and fluoresces green, whereas at a higher membrane potential the JC-1 dye forms polymeric aggregates and fluoresces red. A fall in the mitochondrial membrane potential is therefore indicated by a decrease in the ratio of red signal to green signal.

Cells were cultured in 96 well black culture plates at a density of $8.4 \times 10^3$ cells/well and exposed to various concentrations of Fe-NTA the following day, the medium was replaced with fresh medium containing the same component every 24 h. After six days, the culture medium was replaced with 200 μl JC-1 solution (10 μg/ml JC-1 in HBSS), and cells were incubated in the dark for 30 min at 37 °C. After washing twice with HBSS, the absorbance of the cells in each well was immediately measured using a fluorescence plate reader with the excitation and emission wavelengths set at 490 nm and 530 nm (green)/590 nm (red), respectively.

*Animals.* The production of transgenic mice expressing the HCV core protein has been described previously (Moriya et al., 2001). Briefly, the HCV core protein gene was placed downstream of a transcriptional regulatory region from the hepatitis B virus and introduced into C57BL/6 mouse embryos (Clea Japan, Tokyo, Japan). All of the animals were treated humanely in accordance with the guidelines issued by the National Institute of Health and all procedures described below were approved by the animal care committee of Chiba University.

*Isolation of mouse liver mitochondria.* The mouse liver mitochondrial fraction was prepared according to a previously described method (Masubuchi et al., 2002). Livers were isolated from two mice and placed in ice-cold buffer containing 250 mM sucrose, 10 mM HEPES–KOH, and 0.5 mM EGTA (pH 7.4). Livers were cut into small cubes with scissors in the same buffer and homogenized five times with a Potter homogenizer. The homogenates were diluted to 0.25 g liver/ml and were centrifuged at 770 ×*g* for 5 min at 4 °C. The resulting supernatant was decanted and further centrifuged at 9800 ×*g* for 10 min. The pellet was resuspended to yield a concentration of 0.5 g liver/ml in buffer containing 250 mM sucrose, 10 mM HEPES–KOH and 0.3 mM EGTA (pH 7.4), and centrifuged at 4500 ×*g* for 10 min. The pellet was resuspended to yield a concentration of 1 g liver/ml in the same buffer and centrifuged at 2000 ×*g* for 2 min, followed by further centrifugation at 4500 ×*g* for 8 min. The

final pellet was then resuspended in buffer containing 250 mM sucrose and 10 mM HEPES–KOH (pH 7.4) and used for further experiments.

*Mitochondrial iron uptake.* All experiments were conducted in a 30 °C water bath. After pre-incubation of the mitochondria in buffer containing 225 mM sucrose, 10 mM KCl, 5 mM $MgCl_2$, 5 mM $KH_2PO_4$, and 20 mM Tris–HCl (pH 7.4) for 1 min, Ru360 was added at a final concentration of 10 μM, $^{59}FeSO_4$ was added after 1 min, and the $^{59}Fe$ remaining in the mitochondria after 10 min was measured using a gamma counter.

*Western blotting analysis.* The mouse liver mitochondrial fraction (10 μg protein) was subjected to electrophoresis on a 12.5% polyacrylamide slab gel containing 0.1% sodium dodecyl sulfate and transferred onto an Immobilon-P Transfer Membrane filter (Millipore Corporation, Billerica, MA). The membrane was blocked for 1 h at room temperature with Tris-buffered saline/0.05% Tween 20 (TTBS) containing 3% bovine serum albumin (BSA) and probed overnight at 4 °C with the CCDC109A goat polyclonal IgG (1:200) against the $Ca^{2+}$ uniporter and the ANT goat polyclonal IgG (1:1000). The membrane was then incubated for 1 h at room temperature with donkey anti-goat IgG-HRP (1:3333). All antibodies were diluted in TTBS containing 0.1% BSA. Immunoreactive bands were detected using a LAS-1000 imaging system (Fuji Film, Tokyo, Japan) and an enhanced CL system (GE Healthcare, Little Chalfont, Buckinghamshire, UK).

*Statistical analysis.* All data are represented as the mean ± the standard error (S.E.). Data were statistically analyzed by using one-way ANOVA followed by the Bonferroni test for multiple comparison. For comparison among two groups, two-tailed Student's t-test was adopted. Differences between means at the level of $P < 0.05$ were considered significant.

## Results

### *Iron-induced cytotoxicity in HCV core protein-expressing HepG2 cells*

The iron uptake system is perturbed in HCV-infected hepatocytes due to elevated expression of transferrin receptor 1. However, because of its hydrophobicity, Fe-NTA is taken up into the cell in a transferrin receptor 1-independent manner by passive diffusion. Fe-NTA is then converted into free $Fe^{2+}$ by several types of esterases. Therefore, Fe-NTA was used in the current study to control for intrinsic differences in active iron uptake between HCV core protein-expressing HepG2 cells (Hep39b cells) and vector-transfected HepG2 cells (Hepswx cells). After treatment with Fe-NTA for six days, cytotoxicity was assessed using the MTT assay. Concentration-dependent cytotoxicity of Fe-NTA against Hep39b cells was observed. By contrast, no cytotoxicity was observed against control Hepswx cells at Fe-NTA concentrations of less than 1000 μM (Fig. 1). These data indicate that HCV core protein expression affects the susceptibility of hepatocytes to Fe-NTA-induced iron cytotoxicity.

### *Effect of iron accumulation on ROS production in HCV core protein-expressing versus control hepatocytes*

To directly measure free radical formation, we took advantage of methodology for measuring spontaneous CL and compared the levels of CL in HCV core protein-expressing Hep39b and control Hepswx cells (Fig. 2a). As shown in Fig. 2a, spontaneous CL was significantly higher in Hep39b cells by approximately 156% compared with that in Hepswx cells (6015 versus 3856 arbitrary units; $P < 0.01$). In the presence of 300 μM Fe-NTA, iron-induced CL was also significantly higher in Hep39b cells relative to Hepswx cells (2.61-fold versus 1.54-fold increase; $P < 0.01$ and $P < 0.001$, respectively) (Fig. 2a).

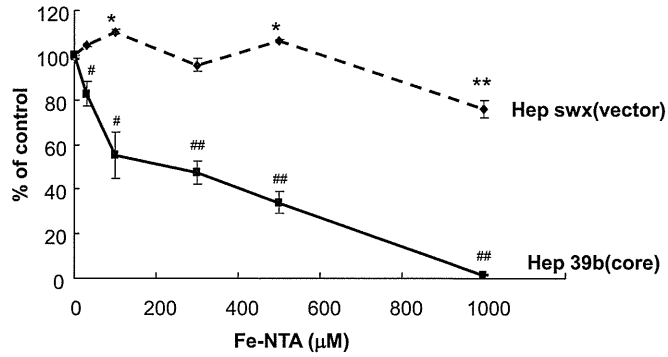


**Fig. 1.** Iron-induced cytotoxicity in control versus HCV core protein-expressing hepatocytes. Hepswx (dashed line) and Hep39b (solid line) cells were exposed with Fe-NTA (30, 100, 300, 500 and 1000 μM) for six days. Hepatotoxicity was determined using the MTT assay. Viability was calculated as the absorbance of the experimental sample relative to that of the controls (without Fe-NTA treatments). Values are the mean ± the S.E. $^{*}P < 0.05$ and $^{**}P < 0.01$, significantly different from the control (without Fe-NTA). $^{\#}P < 0.05$ and $^{\#\#}P < 0.01$, significantly different from respective control cells (Hepswx) ($n = 6$).

### *Effect of iron accumulation on mitochondrial ROS production*

Mitochondria are a major source of ROS production. Therefore, we next examined the production of mitochondrial hydroxyl radicals by free iron catalyzation (i.e., the Fenton reaction). Since increased production of ROS was observed in Hep39b cells in the presence of Fe-NTA, we next examined mitochondrial ROS production by double staining with MitoTracker® Red (red), a fluorescent probe for the mitochondria, and HPF (green), a fluorescent probe for the selective detection of hydroxyl radicals. As shown in Fig. 2b, a strong fluorescent signal derived from HPF was observed in Hep39b cells in the presence of Fe-NTA. This fluorescence overlapped with that generated by MitoTracker® Red (Fig. 2b). The fluorescent signal derived from HPF in overlapped area was significantly higher in Hep39b cells by approximately 200% compared with that in Hepswx cells (Fig. 2c). These data indicate that mitochondrial hydroxyl radical production was increased in the presence of the HCV core protein and Fe-NTA.

### *Effect of HCV core protein on mitochondrial membrane potential*

The HCV core protein is known to inhibit mitochondrial respiratory complex I activity (Korenaga et al., 2005). Inhibition of complex I leads to ROS formation due to premature electron leakage from the complex. Therefore, we next examined the effect of Fe-NTA on mitochondrial membrane potential in Hep39b cells by using JC-1, a lipophilic cationic dye that selectively enters the mitochondria and reversibly changes color from green to red as the membrane potential increases. Fig. 3 demonstrates that the mitochondrial membrane potential was decreased in HCV core protein-expressing Hep39b cells compared with control Hepswx cells. The decrease in membrane potential was significantly increased following exposure to Fe-NTA (300 and 1000 μM) for six days (Fig. 3).

### *Mitochondrial free iron uptake in HCV core protein-expressing versus control hepatocytes*

Because mitochondrial hydroxyl radical production was increased in the presence of Fe-NTA (Fig. 2), the uptake of free iron into isolated mitochondria was next examined. To ensure a sufficient quantity and quality of the mitochondria for this experiment, mitochondria were isolated from the liver of HCV core protein-expressing transgenic and wild-type (control) mice. Fig. 4 shows that the concentration of mitochondrial free

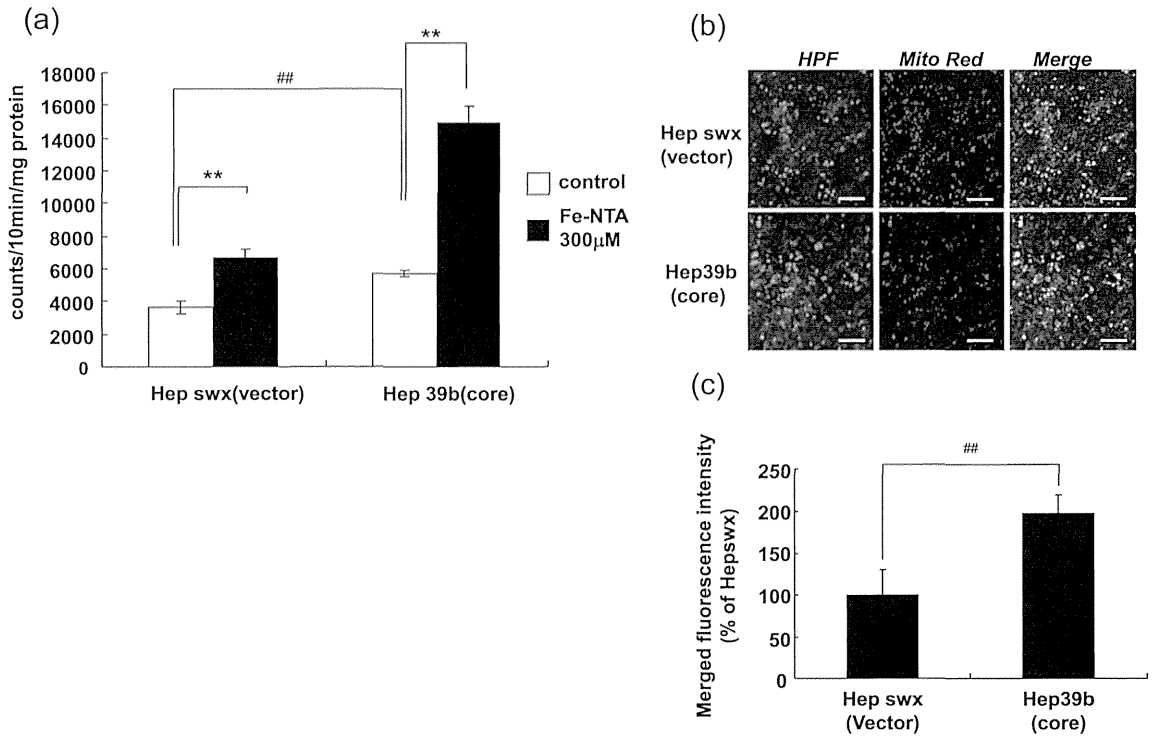


**Fig. 2.** Iron-induced mitochondrial ROS production is enhanced in HCV core protein-expressing hepatocytes. (a) Hepswx and Hep39b cells were exposed to Fe-NTA (300 μM) for six days. ROS production was determined using a CL analyzer. Detected counts were normalized by protein content of cell lysate. Values are given as the mean ± the S.E. $^{**}P < 0.01$ and $^{\#\#}P < 0.01$, significantly different from respective control (n = 3–4). (b) Hepswx and Hep39b cells were pretreated with HPF (green) and MitoTracker® Red (red). Mitochondrial ROS production was determined by the strength of yellow fluorescence in the merged pictures. The scale bar represents 100 μm. (c) Analysis of merged fluorescence microscopy images was done by ImageJ. Integrated density of merged area was automatically selected and fluorescence intensity of HPF was calculated within the merged area of 200–300 cells.

iron ($^{59}Fe^{2+}$) was significantly increased in the mitochondria derived from the transgenic versus the control mouse liver (62.2 ± 4.2 versus 79.5 ± 2.1 pmol/mg protein, respectively; $P < 0.05$), whereas the passive diffusion of $^{59}Fe^{2+}$ into the mitochondria (estimated by $^{59}Fe^{2+}$ uptake at 4 °C) was 31.1 ± 3.2 pmol/10 min/mg protein in Hepswx cells, and 29.2 ± 1.8 pmol/10 min/mg protein in Hep39b cells (not significantly different). Moreover, $^{59}Fe^{2+}$ uptake into the transgenic and control mitochondria was attenuated to the same level by Ru360 (48.2 ± 4.1 versus 47.5 ± 1.2 pmol/mg protein, respectively) (Fig. 4). These data indicate that calcium uniporter plays a role in free iron uptake into the mitochondria and that the activity of the $Ca^{2+}$ uniporter is increased by the HCV core protein.

*Effect of Ru360 on Fe-NTA-induced ROS production and cytotoxicity*

We next examined the effect of Ru360 on Fe-NTA-induced ROS production and cytotoxicity in Hep39b versus Hepswx cells. As shown in Fig. 5a, in the absence of Fe-NTA, Ru360 had no effect on ROS production

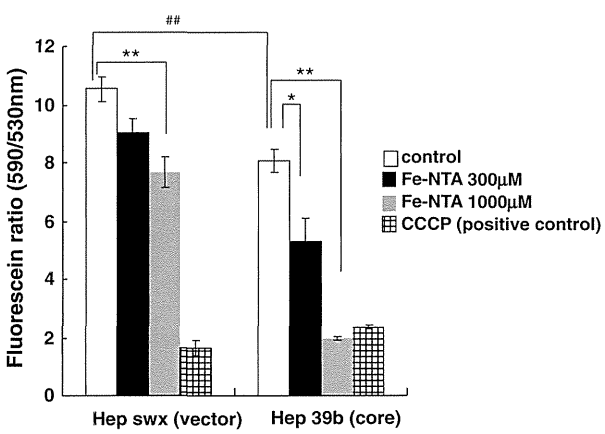


**Fig. 3.** The iron-induced reduction in mitochondrial membrane potential is increased by the expression of HCV core protein. Hepswx and Hep39b cells were exposed to Fe-NTA for six days. Mitochondrial membrane potential was estimated fluorometrically. Values are given as the mean ± the S.E. $^{*}P < 0.05$, $^{**}P < 0.01$ and $^{\#\#}P < 0.01$, significantly different from respective control (n = 6).

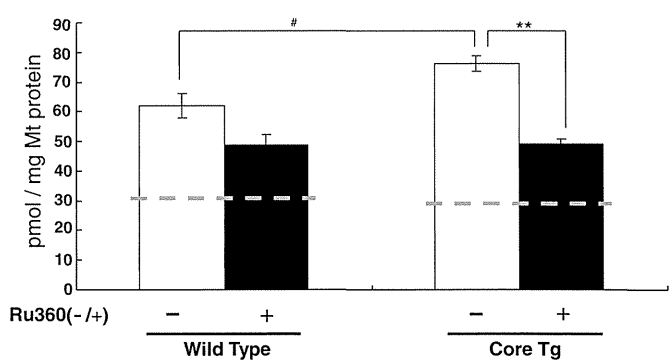


**Fig. 4.** Mitochondrial iron uptake is augmented by the expression of HCV core protein and inhibited by Ru360. Mitochondria were isolated from wild-type and HCV core protein transgenic (Tg) mice and exposed to $^{59}FeSO_4$ with/without Ru360. Free iron uptake was measured in the isolated mitochondria and the free iron uptake amount was normalized by mitochondrial protein content. The dashed line represents the passive diffusion into the mitochondria. Values are given as the mean ± the S.E. $^{**}P < 0.01$ and $^{\#}P < 0.05$, significantly different from respective control (n = 3–8).

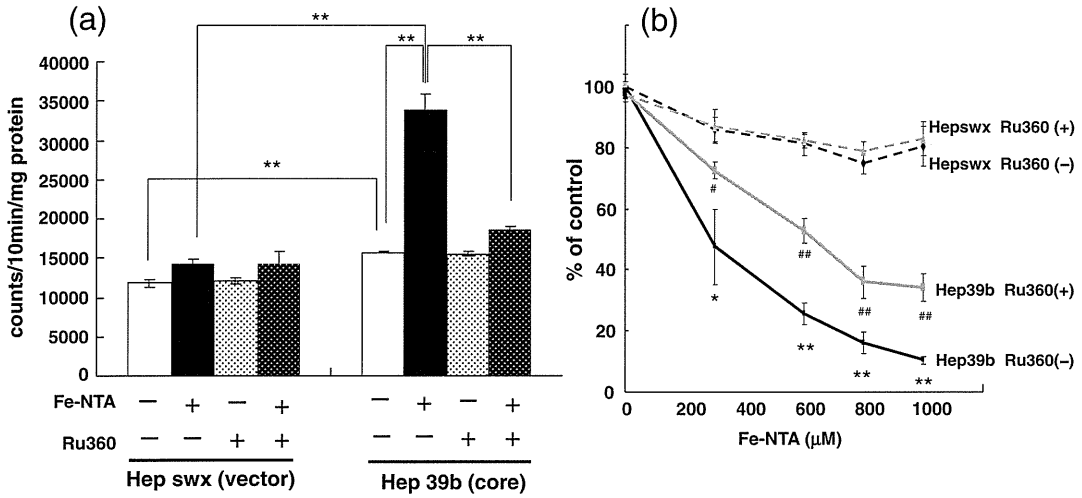


**Fig. 5.** Iron-induced ROS production and cytotoxicity are inhibited by Ru360 in HCV core protein-expressing hepatocytes. (a) Hepswx and Hep39b cells were exposed to Fe-NTA (300 μM) and Ru360 (20 μM) for six days. ROS production was determined using a CL analyzer. Values are given as the mean ± the S.E. **P < 0.01, significantly different from respective control (n = 8). (b) Hepswx and Hep39b cells were exposed to Fe-NTA (300, 600, 800, and 1000 μM) and Ru360 (20 μM) for six days. Cytotoxicity was determined using the MTT assay. Values are given as the mean ± the S.E. *P < 0.05 and **P < 0.01, significantly different from Hepswx Ru360(−). #P < 0.05 and ##P < 0.01, significantly different from Hep39b Ru360(−) (n = 6).

in Hepswx cells and Hep39b cells. On the other hand, Ru360 significantly suppressed Fe-NTA (300 μM)-induced ROS production in Hep39b but not Hepswx cells (Fig. 5a). Moreover, cytotoxicity following exposure to (300, 600, 800 and 1000 μM) Fe-NTA for six days was also specifically inhibited by Ru360 treatment in Hep39b cells (Fig. 5b).

### *Expression of the $Ca^{2+}$ uniporter in isolated mitochondria*

Given that mitochondrial free iron uptake is enhanced in HCV core protein-expressing Hep39b cells (Fig. 4), we next examined the expression of the $Ca^{2+}$ uniporter in the mitochondria isolated from the liver of HCV core protein-expressing transgenic mice relative to control mice. As shown in Fig. 6, mitochondrial expression of the uniporter was similar in transgenic versus control mice, as assessed by Western blot analysis.

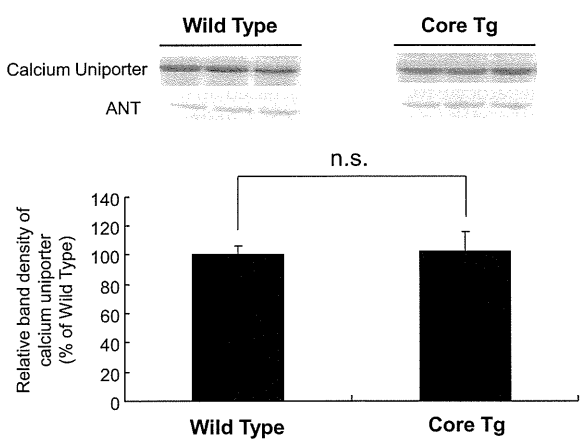


**Fig. 6.** Expression of mitochondrial $Ca^{2+}$ uniporter in the livers of HCV core protein-expressing transgenic versus wild-type mice. Mitochondria were isolated from the livers of wild-type (control) and HCV core protein-expressing transgenic (Tg) mice. The expression levels of the $Ca^{2+}$ uniporter and ANT (loading control) were determined by Western blot analysis. Mitochondrial proteins (10 μg) were loaded into each lane of the gel. The band density of the uniporter was normalized to the band density of ANT. Values are given as the mean ± the S.E. n.s.: not significantly different (n = 3).

## Discussion

The accumulation of iron into the liver of HCV core protein-expressing transgenic mice fed a normal diet is similar to that observed in chronic HCV patients (Farinati et al., 1995; Kato et al., 2001). On the other hand, the expression level of hepcidin, which regulates iron metabolism by inhibiting iron absorption from the intestine and the hepatic portal system, is reportedly decreased in the liver of HCV patients and full-length HCV genome-expressing transgenic mice, but not in the liver of HCV core protein-expressing transgenic mice (Moriya et al., 2010; Muckenthaler, 2008). Therefore, although the precise regulation of iron transport into the mitochondria is essential for heme biosynthesis, hemoglobin production, and Fe–S clustering, the mechanism(s) behind mitochondrial iron homeostasis is not yet fully understood.

Previous work from our group revealed elevated ROS generation in HCV core protein-expressing transgenic mice (Moriya et al., 2001). Moreover, our previous work, along with that of others (Korenaga et al., 2005), showed that the core protein interacts with the outer mitochondrial membrane and impairs the mitochondrial respiratory chain in the normal mouse liver via inhibition of complex I activity (unpublished data). Inhibition of respiratory chain complexes ultimately leads to the overproduction of ROS via electron leakage from the mitochondria. Therefore, we hypothesized that the inducible mitochondrial iron transport system exacerbates hepatic toxicity caused by the HCV core protein.

This study employed Fe-NTA to exclude intrinsic differences in iron uptake into HCV core protein-expressing Hep39b cells and vector-transfected Hepswx cells. In addition, we demonstrated that HCV core protein-induced alterations in mitochondrial ROS production and membrane potential were augmented in the presence of iron (Figs. 2 and 3). These data may indicate that iron-dependent mitochondrial dysfunction was amplified via the Fenton reaction, which produces potent reactive free radicals (i.e., hydroxyl radicals) (Fig. 7).

Iron is absolutely essential for the sustenance of all forms of life due to its unusual ability to serve as both an electron donor and acceptor. On the other hand, free iron is also potentially toxic, which is related to its ability to donate and accept electrons within the cell. Free iron catalyzes the conversion of hydrogen peroxide into free radicals, which can cause damage to the mitochondria and cellular structures. For this reason, the iron homeostasis is strictly regulated, and the impairment of iron homeostasis is related to several diseases. In patients with HCV, hepatic

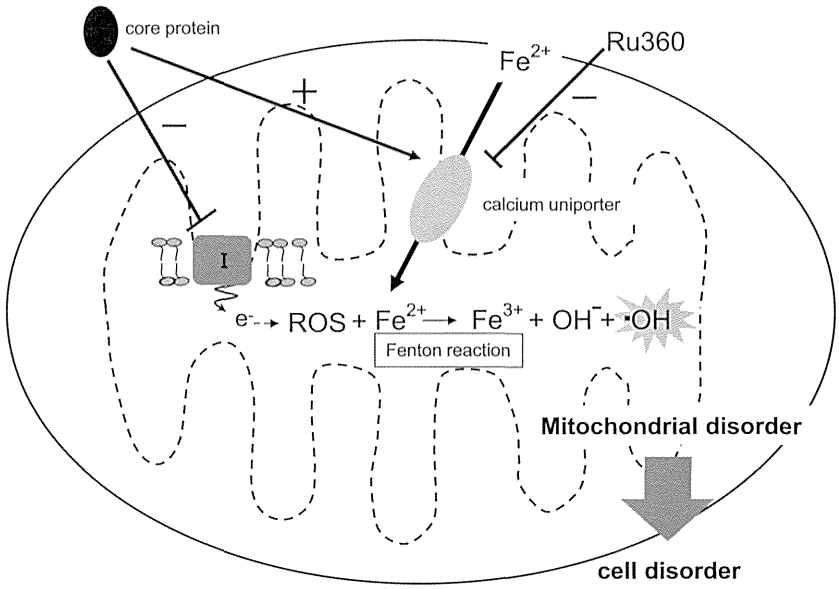


**Fig. 7.** Proposed mechanism of mitochondrial iron accumulation and hepatic cytotoxicity caused by the HCV core protein. The HCV core protein induces mitochondrial ROS production by inhibiting mitochondrial complex I. In addition, it is suggested that the HCV core protein stimulates mitochondrial iron uptake through the mitochondrial $Ca^{2+}$ uniporter. The excess iron then leads to mitochondrial ROS production and mitochondrial/cellular malfunction/disorder when the HCV core protein is expressed.

and serum free iron concentrations are ~7-fold higher (12.5 mmol/g liver and 134 mg/dl, respectively) than those of a normal individual (Farinati et al., 1995; Kageyama et al., 1998; Olynyk et al., 1995; Silva et al., 2005). In this study, significant hepatotoxicity was observed at 30 μM Fe-NTA in HCV core protein-expressing Hep39b cells (Fig. 1). Therefore, a physiologically relevant concentration of iron (30 μM), which is not sufficient to induce cell toxicity by itself, was synergistic with the toxic actions of the core protein (Fig. 1). This interplay was similarly revealed by the synergy between iron and the core protein in inducing mitochondrial dysfunction and ROS production (Figs. 2 and 3).

This study further demonstrated that mitochondrial free iron uptake was partially mediated by the $Ca^{2+}$ uniporter. The $Ca^{2+}$ uniporter was selectively inhibited by Ru360 and exhibited an increased capacity to uptake iron into HCV core protein-expressing liver mitochondria versus normal liver mitochondria (Fig. 4). However, the expression of the uniporter was unaltered in core protein-expressing transgenic mice relative to normal mice (Fig. 6). Li et al. (2007) reported that the activity of the $Ca^{2+}$ uniporter was up-regulated in the presence of the core protein: The in vitro incubation of mouse liver mitochondria with HCV core protein (100 ng/mg) increased the $Ca^{2+}$ entry rate by ~2-fold. The $Ca^{2+}$ uniporter is located in the inner mitochondrial membrane and transports not only $Ca^{2+}$ but also other metal cationic ions (e.g., $Fe^{2+}$) into the mitochondrial matrix space in a mitochondrial membrane potential-dependent fashion (Bernardi, 1999).

Iron uptake was significantly suppressed to the same level by Ru360 in the mitochondria isolated from both core protein-expressing transgenic and normal mice (Fig. 4). Moreover, as free iron uptake into the mitochondria was still observed at 4 °C for both types of the mitochondria, about half of the iron (Hepswx; 31.1 ± 3.2 pmol/10 min/mg protein, Hep39b; 29.2 ± 1.8 pmol/10 min/mg protein) was estimated to enter into the mitochondria by passive diffusion (Fig. 4, dashed line). These data indicate that the up-regulation of iron uptake in the mitochondria isolated from transgenic mice was mediated by the HCV core protein-induced stimulation of Ru360-sensitive $Ca^{2+}$ uniporter transport activity. However, the mechanism by which the core protein alters the function of the mitochondrial uniporter is still unclear, especially given that the core protein binds to the outer mitochondrial membrane, and the uniporter is located in the inner mitochondrial membrane. It is known that mitochondrial calcium uniporter possibly forms multi-molecular complex (Raffaello et al., 2012). Mitochondrial calcium uniporter function could be altered by the effect on essential regulator and/or protein involved in the assembly of the channel. In this regard, though our current study demonstrated that HCV core protein had no effect on $Ca^{2+}$ uniporter expression (Fig. 6), it is possible that other mechanisms are involved in the HCV core protein-induced stimulation of $Ca^{2+}$ uniporter transport activity. Further study should be addressed in the future.

Interferon-α has been used as monotherapy for chronic hepatitis C, yet only about 40–50% of hepatitis C patients experience an initial biochemical response to the cytokine. Interestingly, high iron accumulation in chronic HCV carriers is related to a poor response to interferon therapy (Walters et al., 1973). In addition, some investigators have suggested that iron removal therapy (via phlebotomy or food therapy (i.e., restriction of an iron rich-diet)) can attenuate liver damage in hepatitis C patients by still unknown mechanisms (Hayashi et al., 1994; Kato et al., 2007). The current study showed that the HCV core protein-induced mitochondrial iron uptake is responsible for exacerbating mitochondrial dysfunction and ROS production, which finally seems to lead to hepatocyte toxicity (Fig. 7). Based on these results, we suggest that inhibition of the mitochondrial $Ca^{2+}$ uniporter may provide a new therapeutic approach to treat liver disease in HCV patients.

## Conflict of interest statement

The authors declare no conflict of interest.

## Acknowledgments

This work was supported by a grant-in-aid for scientific research (A) 548 (21249003) and a grant-in-aid for young scientists (B) (21790141) from the Ministry of Education, Culture, Sports, Science and Technology of Japan.

## References

Awai, M., Narasaki, M., Yamanoi, Y., Seno, S., 1979. Induction of diabetes in animals by parenteral administration of ferric nitrilotriacetate. A model of experimental hemochromatosis. Am. J. Pathol. 95, 663–673.

Bartenschlager, R., Lohmann, V., 2000. Replication of hepatitis C virus. J. Gen. Virol. 81, 1631–1648.
Bernardi, P., 1999. Mitochondrial transport of cations: channels, exchangers, and permeability transition. Physiol. Rev. 79, 1127–1155.
Bonkovsky, H.L., Banner, B.F., Rothman, A.L., 1997. Iron and chronic viral hepatitis. Hepatology 25, 759–768.
Bukh, J., Miller, R.H., Purcell, R.H., 1995. Genetic heterogeneity of hepatitis C virus: quasispecies and genotypes. Semin. Liver Dis. 15, 41–63.
Choi, J., Ou, J.H., 2006. Mechanisms of liver injury. III. Oxidative stress in the pathogenesis of hepatitis C virus. Am. J. Physiol. Gastrointest. Liver Physiol. 290, G847–G851.
Farinati, F., Cardin, R., De Maria, N., Della Libera, G., Marafin, C., Lecis, E., et al., 1995. Iron storage, lipid peroxidation and glutathione turnover in chronic anti-HCV positive hepatitis. J. Hepatol. 22, 449–456.
Hayashi, H., Takikawa, T., Nishimura, N., Yano, M., Isomura, T., Sakamoto, N., 1994. Improvement of serum aminotransferase levels after phlebotomy in patients with chronic active hepatitis C and excess hepatic iron. Am. J. Gastroenterol. 89, 986–988.
Ikeda, K., Saitoh, S., Suzuki, Y., Kobayashi, M., Tsubota, A., Koida, I., et al., 1998. Disease progression and hepatocellular carcinogenesis in patients with chronic viral hepatitis: a prospective observation of 2215 patients. J. Hepatol. 28, 930–938.
Kageyama, F., Kobayashi, Y., Murohisa, G., Shimizu, E., Suzuki, F., Kikuyama, M., et al., 1998. Failure to respond to interferon-alpha 2a therapy is associated with increased hepatic iron levels in patients with chronic hepatitis C. Biol. Trace Elem. Res. 64, 185–196.
Kato, J., Kobune, M., Nakamura, T., Kuroiwa, G., Takada, K., Takimoto, R., et al., 2001. Normalization of elevated hepatic 8-hydroxy-2′-deoxyguanosine levels in chronic hepatitis C patients by phlebotomy and low iron diet. Cancer Res. 61, 8697–8702.
Kato, J., Miyanishi, K., Kobune, M., Nakamura, T., Takada, K., Takimoto, R., et al., 2007. Long-term phlebotomy with low-iron diet therapy lowers risk of development of hepatocellular carcinoma from chronic hepatitis C. J. Gastroenterol. 42, 830–836.
Korenaga, M., Wang, T., Li, Y., Showalter, L.A., Chan, T., Sun, J., et al., 2005. Hepatitis C virus core protein inhibits mitochondrial electron transport and increases reactive oxygen species (ROS) production. J. Biol. Chem. 280, 37481–37488.
Kowdley, K.V., 2004. Iron, hemochromatosis, and hepatocellular carcinoma. Gastroenterology 127, S79–S86.
Lau, J.Y., Xie, X., Lai, M.M., Wu, P.C., 1998. Apoptosis and viral hepatitis. Semin. Liver Dis. 18, 169–176.
Li, Y., Boehning, D.F., Qian, T., Popov, V.L., Weinman, S.A., 2007. Hepatitis C virus core protein increases mitochondrial ROS production by stimulation of $Ca^{2+}$ uniporter activity. FASEB J. 21, 2474–2485.
Maeda, T., Miyazono, Y., Ito, K., Hamada, K., Sekine, S., Horie, T., 2010. Oxidative stress and enhanced paracellular permeability in the small intestine of methotrexate-treated rats. Cancer Chemother. Pharmacol. 65, 1117–1123.
Masubuchi, Y., Nakayama, S., Horie, T., 2002. Role of mitochondrial permeability transition in diclofenac-induced hepatocyte injury in rats. Hepatology 35, 544–551.
Moriya, K., Nakagawa, K., Santa, T., Shintani, Y., Fujie, H., Miyoshi, H., et al., 2001. Oxidative stress in the absence of inflammation in a mouse model for hepatitis C virus-associated hepatocarcinogenesis. Cancer Res. 61, 4365–4370.
Moriya, K., Miyoshi, H., Shinzawa, S., Tsutsumi, T., Fujie, H., Goto, K., et al., 2010. Hepatitis C virus core protein compromises iron-induced activation of antioxidants in mice and HepG2 cells. J. Med. Virol. 82, 776–792.
Muckenthaler, M.U., 2008. Fine tuning of hepcidin expression by positive and negative regulators. Cell Metab. 8, 1–3.
Nishioka, K., Watanabe, J., Furuta, S., Tanaka, E., Iino, S., Suzuki, H., et al., 1991. A high prevalence of antibody to the hepatitis C virus in patients with hepatocellular carcinoma in Japan. Cancer 67, 429–433.
Oberley, T.D., 2002. Oxidative damage and cancer. Am. J. Pathol. 160, 403–408.
Okuda, M., Li, K., Beard, M.R., Showalter, L.A., Scholle, F., Lemon, S.M., et al., 2002. Mitochondrial injury, oxidative stress, and antioxidant gene expression are induced by hepatitis C virus core protein. Gastroenterology 122, 366–375.
Olynyk, J.K., Reddy, K.R., Di Bisceglie, A.M., Jeffers, L.J., Parker, T.I., Radick, J.L., et al., 1995. Hepatic iron concentration as a predictor of response to interferon alfa therapy in chronic hepatitis C. Gastroenterology 108, 1104–1109.
Otani, K., Korenaga, M., Beard, M.R., Li, K., Qian, T., Showalter, L.A., et al., 2005. Hepatitis C virus core protein, cytochrome P450 2E1, and alcohol produce combined mitochondrial injury and cytotoxicity in hepatoma cells. Gastroenterology 128, 96–107.
Park, J.S., Yang, J.M., Min, M.K., 2000. Hepatitis C virus nonstructural protein NS4B transforms NIH3T3 cells in cooperation with the Ha-ras oncogene. Biochem. Biophys. Res. Commun. 267, 581–587.
Raffaello, A., De Stefani, D., Rizzuto, R., 2012. The mitochondrial $Ca^{2+}$ uniporter. Cell Calcium 52, 16–21.
Ray, R.B., Meyer, K., Ray, R., 2000. Hepatitis C virus core protein promotes immortalization of primary human hepatocytes. Virology 271, 197–204.
Silva, I.S., Perez, R.M., Oliveira, P.V., Cantagalo, M.I., Dantas, E., Sisti, C., et al., 2005. Iron overload in patients with chronic hepatitis C virus infection: clinical and histological study. J. Gastroenterol. Hepatol. 20, 243–248.
Walters, G.O., Miller, F.M., Worwood, M., 1973. Serum ferritin concentration and iron stores in normal subjects. J. Clin. Pathol. 26, 770–772.
Wang, T., Weinman, S.A., 2006. Causes and consequences of mitochondrial reactive oxygen species generation in hepatitis C. J. Gastroenterol. Hepatol. 21 (Suppl. 3), S34–S37.
Wang, T., Campbell, R.V., Yi, M.K., Lemon, S.M., Weinman, S.A., 2010. Role of hepatitis C virus core protein in viral-induced mitochondrial dysfunction. J. Viral Hepat. 17, 784–793.

World Journal of Gastroenterology

Online Submissions: http://www.wjgnet.com/esps/
bpgoffice@wjgnet.com
doi:10.3748/wjg.v20.i11.3044

*World J Gastroenterol* 2014 March 21; 20(11): 3044-3049
ISSN 1007-9327 (print) ISSN 2219-2840 (online)


CASE REPORT

# Acute hepatitis B of genotype H resulting in persistent infection

Norie Yamada, Ryuta Shigefuku, Ryuichi Sugiyama, Minoru Kobayashi, Hiroki Ikeda, Hideaki Takahashi, Chiaki Okuse, Michihiro Suzuki, Fumio Itoh, Hiroshi Yotsuyanagi, Kiyomi Yasuda, Kyoji Moriya, Kazuhiko Koike, Takaji Wakita, Takanobu Kato

Norie Yamada, Ryuichi Sugiyama, Takaji Wakita, Takanobu Kato, Department of Virology Ⅱ, National Institute of Infectious Diseases, Shinjyuku-Ku, Tokyo 162-8640, Japan
Norie Yamada, Minoru Kobayashi, Kiyomi Yasuda, Department of Internal Medicine, Center for Liver Diseases, Kiyokawa Hospital, Suginami, Tokyo 166-0004, Japan
Norie Yamada, Ryuta Shigefuku, Minoru Kobayashi, Hiroki Ikeda, Hideaki Takahashi, Chiaki Okuse, Michihiro Suzuki, Fumio Itoh, Division of Gastroenterology and Hepatology, Department of Internal Medicine, St. Marianna University School of Medicine, Kanagawa 216-8511, Japan
Hiroshi Yotsuyanagi, Department of Infectious Diseases, Graduate School of Medicine, The University of Tokyo, Tokyo 113-8655, Japan
Kyoji Moriya, Department of Infection Control and Prevention, Graduate School of Medicine, The University of Tokyo, Tokyo 113-8655, Japan
Kazuhiko Koike, Department of Gastroenterology, Graduate School of Medicine, The University of Tokyo, Tokyo 113-8655, Japan
Author contributions: Shigefuku R, Kobayashi M, Ikeda H, Takahashi H, Okuse C, Suzuki M and Itoh F were the patient's attending physicians; Yotsuyanagi H, Yasuda K, Moriya K, Koike K, Wakita T and Kato T organized the study; Yamada N, Sugiyama R and Kato T performed the research; Yamada N and Kato T wrote the manuscript.
Supported by Japan Society for the Promotion of Science and the Ministry of Health, Labour and Welfare and the Ministry of Education, Culture, Sports, Science and Technology of Japan
Correspondence to: Takanobu Kato, MD, PhD, Department of Virology Ⅱ, National Institute of Infectious Diseases, Toyama 1-23-1, Shinjyuku-Ku, Tokyo 162-8640, Japan. takato@nih.go.jp
Telephone: +81-3-52851111 Fax: +81-3-52851161
Received: October 3, 2013 Revised: November 18, 2013
Accepted: December 5, 2013
Published online: March 21, 2014

## Abstract

A 47-year-old man presented with general fatigue and dark urine. The laboratory data showed increased levels of hepatic transaminases. The patient was positive for hepatitis B virus (HBV) markers and negative for anti-human immunodeficiency virus. The HBV-DNA titer was set to 7.7 log copies/mL. The patient was diagnosed with acute hepatitis B. The HBV infection route was obscure. The serum levels of hepatic transaminases decreased to normal ranges without any treatment, but the HBV-DNA status was maintained for at least 26 mo, indicating the presence of persistent infection. We isolated HBV from the acute-phase serum and determined the genome sequence. A phylogenetic analysis revealed that the isolated HBV was genotype H. In this patient, the elevated peak level of HBV-DNA and the risk alleles at human genome single nucleotide polymorphisms s3077 and rs9277535 in the human leukocyte antigen-DP locus were considered to be risk factors for chronic infection. This case suggests that there is a risk of persistent infection by HBV genotype H following acute hepatitis; further cases of HBV genotype H infection must be identified and characterized. Thus, the complete determination of the HBV genotype may be essential during routine clinical care of acute hepatitis B outpatients.



**Key words:** Acute hepatitis; Chronic hepatitis; Genotyping; Hepatitis B virus; Single nucleotide polymorphisms

**Core tip:** Hepatitis B virus (HBV) genotype H infection is rare in Asia, particularly in Japan. Here, we report a case of acute hepatitis B caused by a genotype H strain with persistent infection, although most adult cases of acute hepatitis B are self-limiting in Japan. This case suggests that the HBV genotype H infection can be a risk factor for persistent infection. Therefore, it is necessary to investigate the characteristics of genotype H infection in an accumulation of cases. Thus, the

complete determination of the HBV genotype may be essential in the routine clinical care of acute hepatitis B patients.

Yamada N, Shigefuku R, Sugiyama R, Kobayashi M, Ikeda H, Takahashi H, Okuse C, Suzuki M, Itoh F, Yotsuyanagi H, Yasuda K, Moriya K, Koike K, Wakita T, Kato T. Acute hepatitis B of genotype H resulting in persistent infection. *World J Gastroenterol* 2014; 20(11): 3044-3049 Available from: URL: http://www.wjgnet.com/1007-9327/full/v20/i11/3044.htm DOI: http://dx.doi.org/10.3748/wjg.v20.i11.3044

## INTRODUCTION

Hepatitis B is a potentially life-threatening liver infection caused by the hepatitis B virus (HBV); it represents a major global health problem. HBV can cause chronic liver diseases and increases the risk of death from cirrhosis and liver cancer. Worldwide, an estimated two billion people have been infected with HBV and more than 240 million have chronic infections[1]. The HBV genome consists of approximately 3200-nucleotides of DNA; the virus replicates using a reverse transcriptase enzyme that lacks proofreading ability. Therefore, HBV possesses diverse genetic variability, and the viral population is classified into at least eight genotypes that are designated A -H[2-6]. In Japan, genotypes B and C are prevalent among patients with chronic infections. However, in the last decades, the prevalent genotype in acute HBV infections has shifted from genotype C to A[7-9]. There are some differences in the clinical features and outcomes among the genotypes[10-13]. It has been reported that the persistent infection from acute hepatitis is prevalent in adults that are infected with genotype A HBV. Thus, determining the HBV genotype is of increasing importance even in routine clinical practice, although a reliable kit for determination of all HBV genotypes is still uncommon and is not yet covered by insurance. The host factors associated with persistent infection by HBV have also been reported, such as single nucleotide polymorphisms (SNPs) or genotypes in the human leukocyte antigen-DP locus. It may also be useful for identifying the patients who are prone to develop chronic hepatitis.

In this report, we describe a case of acute hepatitis B resulting from infection by a genotype H strain of HBV. Although the laboratory data and symptoms were not distinguishable from acute hepatitis B with other genotypes, this patient developed persistent infection.

## CASE REPORT

A 47-year-old man living in Kawasaki, Japan, presented at our hospital with general fatigue and dark urine. Approximately 1 wk before visiting the hospital, the patient developed nausea, loss of appetite, and a feeling of fullness in the abdomen. Four days later, he noted darkening of his skin and urine. Upon admission, the patient's laboratory data revealed elevated serum aspartate aminotransferase, alanine aminotransferase (ALT), lactate dehydrogenase, alkaline phosphatase, γ-glutamylt ranspeptidase, and total bilirubin (T-Bil) levels (Table 1). The prothrombin activity was within the normal range (95%). Test for hepatitis B surface antigen (HBsAg; HISCL-2000i, Sysmex, Kobe, Hyogo, Japan), hepatitis B e-antigen (HBeAg; ARCHITECT® CLIA, Abbott Japan, Tokyo, Japan) and anti-hepatitis B core antigen (anti-HBc) IgM (ARCHITECT® CLIA) were positive. A test for HBV-DNA was also positive, exhibiting a titer of 7.7 log copies/mL (COBAS TaqMan HBV Test v2.0, Roche Diagnostics, Tokyo, Japan). HBsAg had not been detected 2 years previously when the patient had been admitted to another hospital for treatment of acute enterocolitis. Other hepatitis virus markers were negative. Therefore, the patient was diagnosed with acute hepatitis B. The genotype of the infecting HBV, as assessed by the Immunis HBV Genotype Immunis® HBV Genotype EIA Kit (Institute of Immunology, Tokyo, Japan), was determined as genotype C. The patient had not been abroad in the past 12 mo; he had no history of receiving blood or blood-related products, transfusions, or drug injections, and he reported no personal or family history of liver disease. The man was unmarried and declared that he was heterosexual, with no history of sexual contact with commercial sex workers or strangers. Anti-human immunodeficiency virus (HIV) was not detected. In the absence of medication, the patient's condition and elevated ALT level improved within a month. Anti-HBe became detectable, and HBeAg disappeared 2 mo after onset of the symptoms. HBsAg became undetectable at 5 mo, but the patient still tested positive for HBV-DNA, a status that persisted for at least 26 mo following his presentation at our hospital (Figure 1). We are now preparing to administer anti-viral medication.

For further analysis of the HBV infecting this patient, HBV-DNA was extracted from the acute-phase serum using a QIAamp DNA Blood Mini kit (QIAGEN, Valencia, CA). The entire HBV genome sequence was determined after polymerase chain reaction (PCR) amplification using the following primers [the number of nucleotides (nt) added to the primers were deduced from the prototype HBV/C clone, with accession no. AB246344]. For the amplification of half of the HBV genome, the outer primers were 5'-ATTCCACCAAGCTCTGCTAGATCCCAGAGT-3' (nt 10-39) and 5'-GGTGCTGGTGAACAGACCAATTTATGCCTA-3' (nt 1813-1784), and the inner primers were 5'-CCTATATTTTCCTGCTGGTGGCTCCAGTTC-3' (nt 46-75) and 5'-TAGCCTAATCTCCTCCC CCAACTCCTCCCA-3' (nt 1760-1731). For the other half of the HBV genome, the outer primers were 5'- ACGTCGCATGGAGACCACCGTGAACGCCCA-3' (nt 1601-1630) and 5'-AAGTCCACCACGAGTCTAGACTCTGTGGTA-3' (nt 266-237), and the inner primers were 5'-CCAGGTCTTGCCCAAGGTCTTACATAAGAG-3' (nt 1631-1660) and 5'-CCCGCCTGTAACACGAGCAGGGGTCCTAGG-3' (nt 207-178). The PCR was performed in a thermal cycler for 30 cycles

**Table 1 Laboratory findings at first visit to our hospital**

| Hematology | | Blood chemistry | | Viral markers | | Immunology | | Coagulation | |
|---|---|---|---|---|---|---|---|---|---|
| WBC | 7400/μL | TP | 7.4 g/dL | Anti-HA IgM | (-) | IgA | 183 mg/dL | PT% | 95% |
| Neutrophil | 72.0% | Albumin | 4.5 g/dL | Anti-HCV | (-) | IgG | 1168 mg/dL | APTT | 36.4 s |
| Eosinophil | 1.0% | T-Bil | 11.1 mg/dL | HBsAg | (+) 197333 | IgM | 220 mg/dL | | |
| Basophil | 0.0% | D-Bil | 8.0 mg/dL | Anti-HBc IgM | (+) 25.5 C.O.I | ANA | × 40, homogeneous | | |
| Monocyte | 10.0% | AST | 1942 IU/L | HBeAg | (+) 253 C.O.I | | | | |
| Lymphocyte | 17.0% | ALT | 2963 IU/L | Anti-HBe | (-) 0.0 % | | | | |
| RBC | 457/μL | ALP | 612 IU/L | HBV-DNA | 7.7 log copies/mL | | | | |
| Hemoglobin | 16.0 g/dL | γGTP | 756 IU/L | Anti-HIV | (-) | | | | |
| Hematocrit | 46.4% | LDH | 739 IU/L | RPR | (-) | | | | |
| Platelet | $36.6 \times 10^4$/μL | BUN | 8.2 mg/dL | TPHA | (+) | | | | |
| | | Creatinine | 0.64 mg/dL | Anti-CMV IgG | (+) | | | | |
| | | T-Chol | 225 mg/dL | Anti-CMV IgM | (-) | | | | |
| | | | | Anti-EBV EBNA | (+) | | | | |
| | | | | Anti-EBV EA IgG | (-) | | | | |
| | | | | Anti-EBV VCA IgG | (+) | | | | |
| | | | | Anti-EBV VCA IgM | (-) | | | | |

WBC: White blood cells; RBC: Red blood cells; ANA: Antinuclear antibody; TP: Total protein; T-Bil: Total bilirubin; D-Bil: Direct bilirubin; AST: Aspartate aminotransferase; ALT: Alanine aminotransferase; ALP: Alkaline phosphatase; γGTP: γ-glutamyltranspeptidase; LDH: Lactase dehydrogenase; BUN: Blood urea nitrogen; T-Chol: Total cholesterol; PT: Prothrombin activity; APTT: Activated partial thromboplastin time; C.O.I: Cutoff index; HA: Hepatitis A; HCV: Hepatitis C virus; HBsAg: Hepatitis B surface antigen; HBc: Hepatitis B core; HBeAg: Hepatitis B e-antigen; HBV: Hepatitis B virus; HIV: Human immunodeficiency virus; RPR: Rapid plasma regain; TPHA: Treponema pallidum hemagglutination assay; CMV: Cytomegalovirus; EBV: Epstein-Barr virus; EBNA: Epstein-Barr virus nuclear antigen; EA: Early antigen; VCA: Viral capsid antigen.

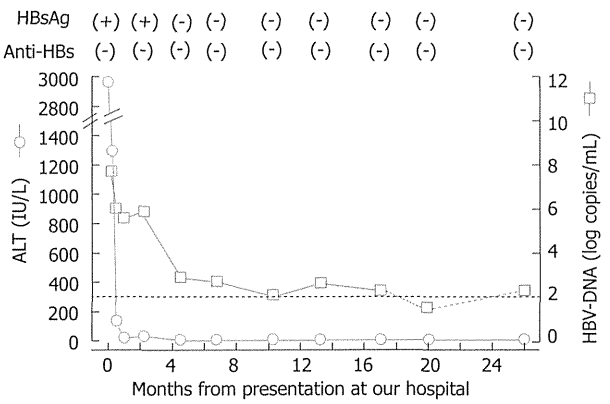


**Figure 1 Clinical course of the patient infected with the genotype H strain.** The dotted line indicates the detection limit of HBV-DNA (2.1 log copy/mL); the titer of the HBV-DNA was below the lower limit at 18 mo. HBsAg: Hepatitis B surface antigen; Anti-HBs: Antibody to hepatitis B surface antigen; ALT: Alanine aminotransferase; HBV: Hepatitis B virus.

(94 ℃, 30 s; 60 ℃, 30 s; 72 ℃, 30 s) with TAKARA LA Taq® DNA polymerase (TAKARA, Shiga, Japan). The amplified fragments were sequenced directly with an automated DNA sequencer (3500 Genetic Analyzer, Applied Biosystems, Foster City, CA, United States).

The genome of the infecting HBV (designated as B-MHJ9014) was 3215 bases in size. A phylogenetic analysis was performed with this strain and several database reference strains. B-MHJ9014 sorted with the genotype-H branch of the tree and clustered with the genotype-H strains previously isolated from Japanese patients (Figure 2). The substitutions at nt 1762 and nt 1764 (the basal core promoter region) and at nt 1896 (the precore region) were not observed. The length of the deduced amino acid sequences of the S, X, Core, and P proteins were identical to those encoded by other genotype H strains in the databases. The α determinant region of the S protein of B-MHJ9014 harbored an amino acid polymorphism (phenylalanine to leucine) at residue 134. The predicted B-MHJ9014 reverse transcriptase did not include any of the amino acid substitutions known to be associated with nucleotide analog resistance. To assess the complexity of the infecting virus, S region sequences from 51 clones in acute phase serum were determined. The detected sequences were genotype H and were closely related to the consensus sequence determine by direct sequencing with 1-3 amino acids polymorphisms (data not shown).

To assess the presence of human genome SNPs in the HLA-DP locus that are associated with persistent infection by HBV[14,15], a blood specimen was obtained from the patient (who had previously provided informed consent). Genomic DNA was extracted from buffy coat samples with the QIAamp DNA Mini kit (QIAGEN); DNA for SNPs rs3077 and rs9277535 were amplified with the appropriate primers and TAKARA LA Taq® DNA polymerase and were sequenced directly. The patient was homozygous (G/G) at both of these SNPs; these alleles are considered to be risk alleles for persistent infection.

## DISCUSSION

HBV genotype H was first reported in 2002[5]. Infections by this genotype have been found mainly in Nicaragua, Mexico, and California; this genotype is considered to be rare in Asia, particularly in Japan[5,16-18]. However, since the first recognition of genotype H in Japan in 2005, eight strains have been isolated from Japanese patients (Table 2)[18-25]. All reported genotype H strains were isolated from male patients aged 35 to 65 years old, and the major route of infection was sexual transmission (5/8, 62.5%). Four cases (50%) represent transmissions that